UPF1 is required for gene expression in mitochondria and for the elimination of paternal mtDNA

Matthew T Wright[1+], Anand K Singh[1,2,3+]*, Hannah L Dixon[1], Emily M Price[1], Elizabeth Connolly[4], Alessandro Di Maio[5], Jonathon Barlow[6], Marco Catoni[1], Yun Fan[1] and Saverio Brogna[1*]

[1]School of Biosciences and Birmingham Centre for Genome Biology (BCGB), University of Birmingham, Edgbaston, Birmingham, B15 2TT, United Kingdom.
[2]Department of Biology, Indian Institute of Science Education and Research (IISER) Tirupati, India, 517619.
[3]Interdisciplinary School of Life Sciences, Institute of Science, Banaras Hindu University, Varanasi, India, 221005.
[4]Department of Biology, Faculty of Science, University of Copenhagen, Universitetsparken 15, Building. 3, 3rd Floor, 2100 Copenhagen O, Copenhagen, Denmark.
[5]Tech Hub Microscopy Facility, College of Medical and Dental Sciences, University of Birmingham, Edgbaston, Birmingham, B15 2TT, United Kingdom.
[6]Cellular Health and Metabolism Facility, School of Sport Exercise and Rehabilitation Sciences, University of Birmingham, Edgbaston, Birmingham, B15 2TT, United Kingdom.

* Correspondance: s.brogna@bham.ac.uk and anandsplash@gmail.com
[+] These authors contributed equally to this work and are considered co-authors.

Abstract

UPF1 is a well-conserved RNA helicase in eukaryotes, involved in nuclear and cytoplasmic processes of gene expression. This study presents ChIP-seq evidence for its RNA-dependent association with mtDNA transcription sites in *Drosophila* S2 cells, and RNA-seq data indicating its requirement for the correct expression of mtDNA genes. UPF1 localisation in mitochondria was observed by immunostaining and GFP-tagging in different fly tissues and cell types. During spermatogenesis, depletion of UPF1 but not of other NMD factors, resulted in major defects in meiosis and cytokinesis, leading to complete sterility. Notably, the few spermatids produced show abnormalities in the formation of the nebenkern and, unlike the wild type, retain the mtDNA.

Introduction

UPF1 is an evolutionary conserved RNA helicase of eukaryotes, which binds both RNA and single-stranded DNA *in vitro* and uses ATP hydrolysis to unfold secondary structures and to dislocate associated proteins (Bhattacharya et al., 2000, Chakrabarti et al., 2011, Czaplinski et al., 1995, Fiorini et al., 2015). UPF1 is commonly found in the cytoplasm where it is associated with mRNA in a translation-dependent manner, and it is most prevalent in the mRNA 3′-UTR (Hogg and Goff, 2010, Hurt et al., 2013, Zund et al., 2013). UPF1 is better known for its role in nonsense mediated mRNA decay (NMD) - a translation-linked process that has been described in all eukaryotes, but the exact mechanism is still insufficiently understood (Brogna and Wen, 2009, Fatscher et al., 2015, Goetz and Wilkinson, 2017, He and Jacobson, 2015, Hug et al., 2016, Karousis et al., 2016, Kim and Maquat, 2019, Lykke-Andersen and Jensen, 2015, Brogna et al., 2016). Besides its activities in the cytoplasm, UPF1 has been recently shown to operate in the nucleus where it associates with nascent RNA to potentially effect transcription and other processes of gene expression in *Drosophila melanogaster* and *Schizosaccharomyces pombe* (De et al., 2022, Singh et al., 2019, Singh et al., 2020). The misregulation of UPF1 is detrimental to cell health, and has been implicated in disease states, such as neurodegeneration and cancers (Zaepfel et al., 2021, Zuniga et al., 2023, Chen et al., 2022, Staszewski et al., 2023). However, it is unclear whether these disease states can be solely explained by increased stability of NMD-dependent mRNA, or are a consequence of specific, NMD-independent functions of UPF1.

The *UPF1* gene was identified in early genetic screens for factors involved in either tRNA suppression, or other translation-related processes in different organisms. Its most frequent name UPF1 (*UP-F*rameshift-*1*) was derived from a genetic screen for co-suppressors of an up-frameshift mutation in *Saccharomyces cerevisiae* (Culbertson, 1999, Leeds et al., 1991). However, *UPF1* was first characterised as *NAM7* (*N*uclear *A*ccommodation of *M*itochondria *7*) in a screen for nuclear genes that, when overexpressed, restore respiration in strains carrying mutations in Group I or Group II introns of mitochondrial genes (Altamura et al., 1992, Asher et al., 1989). Deletion of *UPF1*, *UPF2* and *UPF3*, which all equally inhibit NMD, lead to respiratory impairment in *S. cerevisiae*. However, only *UPF1* overexpression can suppress mitochondrial splicing mutations (de Pinto et al., 2004). Since UPF1 was not detected in *S. cerevisiae* mitochondria, these effects were therefore interpreted to be a consequence of UPF1 overexpression; resulting in the mis-expression of undefined mitochondria residing proteins

involved in splicing (de Pinto et al., 2004). Yet it remains unclear whether a small amount of UPF1 could localise in mitochondria to impact mtDNA gene expression (de Pinto et al., 2004).

In this study, starting with the serendipitous observation that specific regions of the mtDNA are unexpectedly enriched in UPF1 ChIP-seq experiments using *Drosophila* S2 cells, we have investigated whether this protein plays a role in mitochondria. The association with mtDNA genes was confirmed by ChIP qPCR and likely involves binding to the nascent RNA as it is RNAase-sensitive. Furthermore, UPF1 mitochondrial localisation was validated by immunostaining and GFP-tagging in several *Drosophila* tissues, including the salivary gland and indirect flight muscles, with a more detailed examination in spermatogenesis. Throughout the stages of spermatogenesis, UPF1 is as abundant in mitochondria as it is in the cytoplasm, particularly in the nebenkern, a characteristic large structure, formed by the fusion and furling of all mitochondria in the cell, found adjacent to the haploid nucleus in the round spermatid (Fabian and Brill, 2012, Hales and Fuller, 1997). Knockdown of UPF1 (UPF1KD) in mitotic (spermatogonial) cells during early spermatogenesis, causes abnormalities in meiosis and nebenkern formation. The few elongated spermatids that are produced do not develop into mature spermatozoa, leading to complete male sterility. In contrast, knockdown of other NMD factors shows no apparent abnormalities and the flies are fertile. Remarkably, UPF1KD elongated spermatids retain the mtDNA in their axonemal mitochondria, whereas in wild type this is removed by mechanisms that prevent the inheritance of paternal mtDNA. Prior to this investigation, the only proteins implicated were the mitochondrial endonuclease EndoG and mtDNA polymerase POLG1 in *Drosophila* (DeLuca and O'Farrell, 2012, Yu et al., 2017, Lee et al., 2023, Patel, 2017), and mitochondrial transcription factor A (TFAM) in humans (Lee et al., 2023). Our study provides insight into a novel mechanism of paternal mtDNA elimination which requires UPF1 function. Additionally, these data demonstrate an essential role of UPF1 at the different stages of sperm development.

Results

UPF1 is associated with transcription sites of the mitochondrial genome

Whilst re-analysing UPF1 ChIP-seq datasets generated during an earlier study (Singh et al., 2019), we made the unexpected observation that specific regions of the mtDNA are enriched and could therefore, be directly or indirectly associated with UPF1. The enrichment is most apparent for the A-T-rich of the mtDNA, with the first half showing more enrichment than the second (Figure 1A). This region consists of two arrays of highly similar sequence repeats that can be classified into distinct sequence types, one located in the first, and the other in second, which are separated by nonrepetitive sequences (Lewis et al., 1994). The A-T-rich region is the structural equivalent of the D-loop in mammalian mtDNA, which is also known as the major noncoding region (NCR)(Holt and Reyes, 2012). This, in *Drosophila*, contains a unidirectional mtDNA replication origin in its middle, which advances in the direction of rRNA genes (Joers and Jacobs, 2013). The A-T-rich region is flanked by two promoter/transcription start site (TSS) regions which correspond to two major divergent transcription units, containing a cluster of seven protein-encoding genes (TU1), and the other to the small and large ribosomal rRNAs (TU3) and the ND1 gene (Figure 1A)(Torres et al., 2009). The TSS region of the other two divergent transcription units, located between the ND4 and ND6 genes, appear to also be enriched (Figure 1A; TU2 and TU4) (Torres et al., 2009). The enrichment profile is similar between two biological replicates, despite the different overall level of enrichment in the two repeats (Figure 1A, top red graphs). Enrichment of mtDNA is not typically detected in ChIP experiments, for example, there is no evidence of enrichment of these, or the other regions in the Ser2 Pol II ChIP-seq dataset, which was generated in parallel, and similarly aligned (Figure S1A). Likewise, the sequencing of the input sample shows uniform coverage along most of the mtDNA, with somewhat lower coverage at the A-T region, like due to the repetitive structure (Figure 1A, bottom purple graph). Although this region mostly consists of sequence repeats (Figure 1A, horizontal yellow arrows); it should also be noted that the enrichment peaks mostly map in the inter-repeat regions, particularly in the second half of the A-T region (a prominent peak is denoted by the vertical arrow in Figure 1A). This, in conjunction with a lack of enrichment of mtDNA in the Pol II ChIP-seq dataset (including published datasets from other laboratories, which were analysed as a control, Figure S1A), strengthen the interpretation that the binding of UPF1 within this region is unlikely to be a technical artefact associated with the ChIP or the sequence alignment.

The association with the rRNA loci and the ND4 region was also validated by independent ChIP-qPCRs. These show an enrichment profile comparable to the ChIP-seq (Figure S1B; the A-T region could not be tested as specific PCR primers could not be designed due to the high A/T content of the sequence). Additionally, the association with the ND4 and rRNA regions is RNase-sensitive (Figure S1C). The A-T region could not be assessed for RNase-sensitivity; however, mitochondrial transcription promoters are intrinsically bidirectional. Therefore, the A-T region is likely to be highly transcribed from both TU1 and TU3 promoters in the antisense directions. It is feasible that the association of UPF1 with this region is also RNA-dependent. Whether this association could be partially explained by the binding of UPF1 to ssDNA or RNA/DNA hybrids was not investigated. However, neither type of structures are expected to be prevalent in the A-T region of *Drosophila* (Joers and Jacobs, 2013).

UPF1KD affects mtDNA gene expression

Given that UPF1 associates with the transcription sites of mtDNA, it was examined whether UPF1KD results in changes to the expression of mtDNA genes. Initially, RNA-seq analysis in S2 cells showed that 6 of the 15 mtDNA genes (Figure S2A) are downregulated in UPF1KD cells, whilst these show a modest reduction (>0.2 log2 negative fold change), the adjusted P-value (p.adj) calculated for each gene comparison (p.adj ≤0.005) indicates that these are likely significant differences. Notably, the 6 downregulated genes appear to be associated with UPF1 more than other mtDNA genes in control cells; a striking example is ND4 (Figure 1A). Next, we examined UPF1KD salivary glands, by RNA-seq. This also indicates downregulation (a more pronounced >1.5 log2 negative fold change) for several mtDNA genes (Figure S2A). For 8 of these the P-value is ≤0.05, and for 4 of these the adjusted P-value is around the 0.05 threshold (Figure S2B, see Materials and Methods). Whilst the statistical significance of these changes is not as convincing as in S2 cells, similar RNA-seq analysis in UPF2KD and UPF3KD salivary glands shows no evidence of any downregulation (Figure S2C and S2D). Instead, in UPF2KD there is evidence for a significant upregulation of 2 mtDNA genes (Figure S2C, this was not investigated further). Therefore, the trend of downregulation in mtDNA gene expression seems to be specific to UPF1KD, and cannot be explained by a reduced mtDNA copy number in either cell type (see data provided below).

Microscopic visualisation of UPF1 within mitochondria

UPF1 could also be detected in mitochondria by immunostaining of S2 cells (Figure 1B). This showed a punctate signal that is most intense in the cytoplasm, yet some of the UPF1 foci are localised within the mitochondria, identified by staining the cells prior to fixation with a fluorescently conjugated dye which accumulates in the matrix of functional mitochondria (MitoSpy; Material and Methods). Additionally, UPF1 foci within the mitochondria often colocalise with DAPI stained regions (Figure 1B, panels II-IV, magnified views of a mitochondrion, the arrow point to one of these foci), which are likely to correspond to nucleoids – clusters of multiple mtDNA molecules (Bogenhagen, 2012).

Purification of mitochondrial fractions from S2 cells, followed by western blotting also indicates that a portion of UPF1 is copurifying with cytochrome c oxidase subunit 4 (COX4; a component of the respiratory chain located in the inner mitochondrial membrane). Whereas, α-tubulin is hardly detectable, indicating these mitochondrial fractions having minimal cytoplasmic contaminants (Figure S3A).

Next, we examined whether UPF1 can be detected in salivary glands, as these are large cells ideal for microscopic imaging. Here it was found that a portion of UPF1 can also be detected within the mitochondria by both immunostaining of endogenous UPF1, and by imaging of a transgenic GFP-tagged UPF1. The latter was expressed using the UAS-GAL4 system and the salivary gland specific GAL4 driver (*FkhGAL4*). Immunostaining of endogenous UPF1 shows strong and profuse signals in the cytoplasm, and to a smaller extent, within mitochondria demarcated COX4 signal (Figure S4A, the inset shows a magnified view of UPF1 signals in DAPI stained regions). The mitochondrial localisation is also apparent in third instar larval glands, at this stage of development the cells are replete with large secretory vesicles (Figure S4B). The transgenic GFP-UPF1, which is overexpressed relative to the endogenous protein (Singh et al., 2019), at high magnification displays a punctate pattern, with foci of variable size and brightness. GFP-UPF1 foci can also be detected within mitochondria (Figure S5A, panels V-VIII show a strong GFP-UPF1 dot which colocalises with DAPI).

Prominent UPF1 mitochondrial localisation in flight muscles

UPF1 mitochondrial localisation is strikingly prominent in adult flight muscles. These are characterised by distinctive rows of large, tubular, fused mitochondria, located between the myofibrils. Both immunostaining of endogenous UPF1 (Figure 2A), and imaging of transgenic

GFP-UPF1 expressed in the muscle (Figure 2B), using the *MhcGAL4* driver (Materials and Methods), shows that UPF1 appears to be relatively more abundant within mitochondria than cytoplasm. Regions of cytoplasm can be distinguished as spaces between myofibril bundles that are not occupied by mitochondria, such as the region indicated by the dashed yellow rectangle Figure 2A, panel I-II. Bright dots of the UPF1 signal are often detected within mitochondrial regions that do not stain for COX4 (Figure 2A, panels IV-VI). These possibly correspond to nucleoids, but it could not be verified by DAPI staining in these preparations. The mitochondrial localisation is striking apparent when GFP-UPF1 is expressed alongside the UAS-mCherry-mito transgene (see Material and Methods), in which most of the protein appears predominately localised within the mitochondria, with only a small portion present in the cytoplasm (Figure 2B, panels I-II, a region corresponding to the cytoplasm indicated by yellow dashed line).

UPF1 mitochondrial localisation is dynamic in spermatids

To further investigate UPF1 mitochondrial localisation, and its putative role in mitochondrial function, we examined the *Drosophila* testes. These contain cells with characteristic large mitochondrial structures which are a consequence of major morphological changes during spermatogenesis. Spermatogenesis starts with a germline stem cell that, after four cycles of mitosis, generates 16 primary spermatocytes, which produce 64 haploid spermatids following meiosis. Both cell types have recognisable mitochondrial structures. These are the mitoball, a recently described, transient cluster of mitochondria in pre-meiotic spermatocytes (Li et al., 2023); and the nebenkern, a large round structure adjacent to the nucleus of round spermatids, which is formed by fusion of all mitochondria within these cells (Figure 3A)(Hales and Fuller, 1997). We first examined the subcellular localisation of endogenous UPF1 by immunostaining testes ubiquitously expressing mito-mCherry as a mitochondrial marker (*ubi-mito-mCherry*) (Lee et al., 1988). This shows punctate staining with as much signal in the mitochondria, as in the cytoplasm in most cell types (Figure 3B-D). This can be observed in both the mitoball (Figure 3B), and the nebenkern (Figure 3C). A similar pattern was seen in the axonemal mitochondria of elongating spermatids (Figure 3D). However, UPF1 signals are absent in the axonemal mitochondrial derivatives of fully elongated spermatids (Figure 3E, panels II and IV). These also lacked DAPI foci in their tail (Figure 3F, panel V), consistent with the expectation of paternal mtDNA elimination prior to the full elongation of the spermatid.

We also examined the subcellular localisation of transgenic GFP-UPF1 alongside mito-mCherry using the cell-specific driver *bamGAL4*:*VP16* (*bamGAL4*), which starts to be highly expressed in early spermatogonial cells (White-Cooper, 2012). GFP-UPF1 showed a localisation pattern similar to the endogenous protein (Figure S6). In primary spermatocytes, strong signals were detected both in the cytoplasm, the mitoball region (Figure S6A, panels II and IV) within the nebenkern (Figure S6B, panel IV). Whilst, only residual, just above background, GFP-UPF1 signal could be detected within the axonemal mitochondria of elongated spermatids (Figure S6E, panel IV).

This set of observations demonstrate that UPF1 localises to mitochondria in both primary spermatocytes and developing spermatids, and that UPF1 signals are distributed throughout the mitochondria including in the nucleoid regions. The exception is fully elongated spermatids where neither UPF1 nor nucleoid/mtDNA signals are present. It seems, therefore, that the localisation of UPF1 in mitochondria correlates with mtDNA presence in spermatids.

UPF1KD impairs meiosis and nebenkern formation

Given the mitochondrial localisation of UPF1 in the nebenkern, we examined what the consequences of knockdown would be for the developing spermatids, as the nebenkern is required for the correct development of mature spermatids (Noguchi et al., 2011). In wild type, the nebenkern is found adjacent to the nucleus of the four gametes at the round spermatid stage (Figure 4A, panel I). However, in UPF1KD testes at this stage, most nuclei lack the adjacent nebenkern, between the four haploid spermatids there is a single, abnormal, giant nebenkern (Figure 4B, panels I-III). Although, a syncytium-like appearance can also frequently be observed in wild type with this type of preparation (Figure 4A, panel II), consistent previous reports (Hales and Fuller, 1997), groups of four clearly distinguishable round spermatids were not observed in UPF1KD testes. Therefore, the syncytium appearance and the formation of a single giant nebenkern is likely a consequence of incomplete cytokinesis, the fusion of all mitochondria from all four spermatids. Additionally, the different size nuclei suggest chromosomal segregation defects, as previously as previously reported for meiotic mutants (Giansanti et al., 2012, Giansanti and Fuller, 2012).

Quantification of the nebenkern area in wild type and UPF1KD spermatids reveals that the two-dimensional area of the nebenkern in UPF1KD spermatids is approximately 3.3-fold larger than that of wild type round spermatids (Figure 4C). Implying that the volume is more than 4-

fold greater than that of a normal nebenkern. As a result, it is likely less compact, consistent with its appearance (Figure 4A vs 4B). This giant nebenkern shows additional structural abnormalities, including spheroid bodies within the giant nebenkern (Figure 4B, indicated by arrowheads in panel III). These have the appearance of membrane bound vacuole-like compartments and could potentially represent cytoplasmic inclusions. Similar to those previously described in spermatogenesis mutants which affect nebenkern formation (Dorogova et al., 2013). However, these spheroid-bodies that have been described seem larger in size, and are not destroyed by the pressure applied during the testes squashing preparation procedure. Therefore, they must be bound by a stiff membrane or double membrane enclosure. It is not likely to be nuclei though, as they do not contain any DNA (Figure S7). Additionally, no MitoTracker (mitochondrial dye similar to MitoSpy) signal can be detected within (Figure S7), perhaps suggesting that these bodies are large mitochondrial-fusion derivatives that no longer have functional polarised membranes. In size and shape they are reminiscent of the enigmatic giant mitochondria observed by TEM in human pathologic cells (Shami et al., 2023).

Presence of protrusions at the periphery of the late nebenkern in wild type but not UPF1KD

Unexpectedly, two different types of nebenkern could be distinguished in wild type round onion-stage spermatids (Figure 5A), here mitochondria are labelled by endogenously expressed GFP-tagged TFAM (*BAC-TFAM-GFP*). TFAM is the mitochondrial transcription factor A, which binds mtDNA and plays a key role in packaging it into a nucleoid, and it can serve as a marker of nucleoid localisation (Kukat et al., 2015, Kaufman et al., 2007). The first, early-stage, displayed an oblong shape, in which there are visible layers of the mitochondrial derivatives (Figure 5A, panels I-III). The second, late-stage, were circular in shape (Figure 5A, panels IV-VI). Different types of the nebenkern could not be distinguished in UPF1KD though (Figure 5B). Notably, it appears that there is 1.5-fold more mtDNA (corresponding to the corrected total DAPI fluorescence signal within the nebenkern region; see Material and Methods) in the late-stage compared to the early-stage (Figure 5C), consistent with mtDNA replication that occurs during the later stages of nebenkern formation (Yu et al., 2017). Expectedly, in the UPF1KD nebenkern there is 5.38-fold and 3.45-fold more mtDNA compared to the early and late nebenkern in wild type, respectively (Figure 5C). This is consistent with the expectation that all mitochondria within the four UPF1KD round spermatids fuse to form this abnormal nebenkern.

Protruding structures often containing mtDNA were observed at the periphery of the apical side of late nebenkern in wild type (Figure 5D, panel I-IV). However, no such structures were found in the UPF1KD nebenkern, nor is there mtDNA in the large spheroid bodies, described above (Figure 5B, panel III; Figure S7).

UPF1KD but not that of other NMD factors causes male sterility

As abnormalities in meiosis and cytokinesis were observed, we also investigated whether depletion of UPF1 affected male fertility. We examined fertility of flies depleted of UPF1, UPF2, UPF3 and SMG5 (data not shown) during spermatogenesis using *bamGAL4*-driven RNAi. UPF1KD using two independent RNAi lines (see materials and methods) showed complete male sterility, while that of UPF2KD, and UPF3KD resulted in fertile males (Figure 6A); SMG5KD also did not affect male fertility (unpublished data). In wild type, the seminal vesicle is full of mature sperm (Figure 6B, Panels I-III), however, in UPF1KD testes none is observed (Figure 6B Panels, IV-VI, RNAi$^{(1)}$; and Figure 6C, panels I-III, RNAi$^{(2)}$). Inversely, sperm is detected in the seminal vesicle of UPF2KD and UPF3KD testes (Figure 6C, Panels IV-IX). The sterility in UPF1KD is primarily due to the absence of mature sperm. It seems, therefore, that the few spermatids that are produced must be eliminated at a later stage of differentiation.

UPF1KD prevents paternal mtDNA elimination

Despite the major disruption in spermatogenesis, elongated spermatids are produced in UPF1KD testes (Figure S8). Although we found no evidence of individualisation complex formation in UPF1KD (unpublished), these spermatids incorporate GFP-tagged Don Juan (Figure S8). This protein is a marker of elongating, and fully elongated spermatids (Santel et al., 1997). Notably, unlike in wild type, multiple clusters of DAPI signal could be detected in UPF1KD and are evenly distributed throughout the spermatid tails, in which the bundle of spermatids we have compared appear to be at a similar developmental stage, based on nuclei morphology (Figure 7, panels III-IV). The DAPI signals in UPF1KD likely represent mtDNA/nucleoids, which are absent in wild type, at a similar stage of elongation (Figure 7, panel I and II). In view of the apparent defects in chromosomal segregation described above, it was considered whether these could instead be fragments of chromosomal DNA. To distinguish between these two explanations, we utilised *BAC-TFAM-GFP*. This examination showed that TFAM is diffuse in wild type mature sperm tails (Figure S9, panels IV-V), while

dots that colocalise with DAPI signals are present throughout the entire tail in UPF1KD spermatids (Figure S9A, panels IX-X). The level of TFAM-GFP is higher in UPF1KD, and this is in part, due to transcriptional up-regulation (Figure S9B-C). The level of TFAM in *BAC-TFAM-GFP* will be greater than in the originating line, due to an additional endogenous locus, this implies that overexpression of TFAM is not likely to cause mtDNA retention. Additionally, no evidence of TFAM/mtDNA foci were observed in neither UPF2KD nor UPF3KD spermatids (Figure S9, RNAi efficiency of each line was experimentally verified, see figure legend).

The mtDNA copy number was also quantified by qPCR in wild type, and UPF1KD testes. This analysis indicates that UPF1KD testes carry 3-fold more mtDNA compared to wild type (relative to the autosomal genomic locus: *RpL32*). This increase is apparent in pre-eclosed and eclosed males, with a greater increase seen in the eclosed males (Figure 7B and C, respectively). However, in UPF1KD salivary glands (Figure 7D) and S2 cells (Figure 7E), there is no change to the number of mtDNA copies relative to wild type. Therefore, this seems consistent with the interpretation that mtDNA/nucleoids are only retained in the UPF1KD elongated spermatids.

Discussion

The findings presented here offer evidence that the RNA helicase UPF1 enters mitochondria and becomes associated with mtDNA. This conclusion is drawn from several experimental observations, including ChIP-Seq data from *Drosophila* S2 cells, revealing an association with mtDNA transcription sites and possibly also with the A-T rich major noncoding region. At these sites, the association is most apparent at promoter-proximal regions, likely reflecting an association with nascent RNA, as indicated by RNase-sensitive ChIP-qPCR experiments. UPF1 was also visually detectable in mitochondria via immunostaining, and by the expression of a transgenic GFP-tagged variant in different *Drosophila* cell types. In most cells examined, UPF1 is less abundant in mitochondria compared to the cytoplasm. However, in muscles, a higher level of UPF1 was observed in the mitochondria than the cytoplasm, and in spermatids, the level in the mitochondria is similar to that of the cytoplasm.

The *Drosophila* UPF1 sequence lacks an N–terminal mitochondrial targeting signal (MTS) and is not predicted to localise to mitochondria by computational methods, based on published data (Chacinska et al., 2009, Fukasawa et al., 2015, Savojardo et al., 2020). However, this is not uncommon, as several core mitochondrial proteins do not possess an MTS, and their localisation cannot be predicted from the primary sequence (Bader et al., 2020). For example, about 25% of yeast mitochondrial ribosomal protein (MRPs) do not possess a classic MTS (Bykov et al., 2022). UPF1 could be categorised as a dual-localised protein, or even more accurately, given its localisation in the nucleus and the cytoplasm, a tri-localised protein. However, identifying the sequences mediating this localisation will require experimental investigation, possibly using microscopy approaches (Bader et al., 2020).

Here we have examined the mitochondrial role of UPF1 in spermatogenesis. Our data demonstrates that UPF1, but not UPF2 and UPF3, are essential for spermatogenesis. Multiple observed abnormalities in spermatids could account for sterility, including abnormal chromosomal segregation during meiosis, and incomplete cytokinesis. Due to incomplete cytokinesis during meiosis, rather than the formation of a single nebenkern adjacent to each of the four haploid nuclei, a giant nebenkern is only seen adjacent to one of the four nuclei. This giant nebenkern probably forms from the cumulative fusion of mitochondria from all four spermatids, as their cytoplasm is likely to remain connected, as previously reported for meiotic and cytokinesis mutants (Giansanti et al., 2012, Giansanti and Fuller, 2012). Despite these abnormalities, some elongated spermatids are generated. Given that the nebenkern is necessary

for elongation (Noguchi et al., 2011), there is a possibility that only 25 % of the expected number are generated. Yet, these must be eliminated at a later stage, as no mature sperm is observed in the seminal vesicle.

Notably, an additional phenotype could be seen in the elongated spermatids in UPF1KD: the retention of mtDNA, which is normally removed in wild type. It is instead retained in their tails. The function of UPF1 in mitochondrial processes that rationalises its requirement in removing mtDNA/nucleoids will need to be investigated in the future. We would like to draw attention though, to as far as we know, previously unreported protrusions that are observed in the periphery of the wild type, late nebenkern. Two types of nebenkern could be distinguished in this study, termed early- and late-stage, likely representing distinct stages of nebenkern formation and maturation. These protrusions were observed only in the late-stage and appear to often contain mtDNA (Figure 5D, panels I-IV). Similar structures were not observed in the nebenkern of UPF1KD spermatids, and the spheroid bodies which are present in these abnormal nebenkerns contain no DNA (Figure S7B, panels I-III), while the rest of the nebenkern has between 3.45- and 5.38-fold more mtDNA than in wild type. As these protrusions in wild type contain mtDNA, they could represent structures which extrude mtDNA from the late nebenkern. It is, therefore, plausible that the elimination of mtDNA from the spermatid could take place in two stages. In the first stage, some of the mtDNA eliminated via some type of “exomytosis” mechanism involving the formation of nebenkern protrusions. This mechanism could perhaps be analogous to those which extrude mtDNA during inflammation. This early elimination of mtDNA at the nebenkern stage, could be mechanistically distinct from those that operate in the elongated spermatids, which, as previously described, are thought to involve putative clipping/degradation/deprotection of the mtDNA in the elongated axonemal mitochondria (DeLuca and O'Farrell, 2012, Yu et al., 2017, Lee et al., 2023, Patel, 2017). The extrusion of mtDNA has been proposed to occur under pathological conditions in mammalian cells, in which the presence of cytosolic mtDNA triggers the cGAS-STING pathway, an inflammatory response part of the native immune system (Kim et al., 2023, Riley and Tait, 2020). Interestingly, knockdown of the mtDNA polymerase and TFAM inhibits this inflammatory response. This would suggest that TFAM-driven compaction is required for mtDNA bulk extrusion (Kaufman et al., 2007, Kukat et al., 2015). UPF1 association with mtDNA could be playing a similar role.

Given that UPF2, UPF3 and SMG5 are not required for spermatogenesis, the role that UPF1 plays in this process is independent of NMD in *Drosophila.* This conclusion differs from that of previous studies which have concluded that the modulation of NMD-dependent mRNA stability is required for spermatogenesis in mice, and other organisms (Bao et al., 2016, Fanourgakis et al., 2016, Han et al., 2018, Lehtiniemi et al., 2022).

Our data also indicate that at least 6 mtDNA genes are downregulated in UPF1KD S2 cells. The adjusted P-value associated with each gene comparison is ≤0.005, so the probability that 6 of 15 mtDNA genes (out of a total of 17610 genes analysed) are mis-regulated by chance is in the order of 1.6×10^{-15} [$(1/200)^6$]. It appears, therefore likely, that UPF1 is required for correct mtDNA gene expression. However, whether this is the direct consequence of UPF1 association with the nascent RNAs, will need to be investigated in future studies, to determine whether it could affect transcriptional and post-transcriptional mitochondrial processes. In support of this, 6 genes that are downregulated in UPF1 S2 cells are also those most associated with UPF1 by ChIP; a striking example is ND4 (Figure 1A). Given that UPF1 is likely to be involved in the expression of a large fraction of the nuclear genome, the alternative hypothesis is that these changes could be linked to the misexpression of some other nuclear genes that are involved in mtDNA gene expression. Additional RNA-seq analysis did not identify this to be the case (not shown, information can be extracted gene counts files deposited on GEO: GSE266138).

Cumulatively, the data we have discussed here further reinforce the notion that UPF1 plays broader role in gene expression, extending to the mitochondria. Therefore, it is possible that misregulation of the mitochondrial genome partially contributes to the phenotypes associated with UPF1 dysfunction shown here, and those previously associated with disease states.

Materials and Methods

Cell Culture, RNAi interference and immunostaining

S2 cells (CVCL_Z232) were cultured in Schneider's insect cell culture media (Catalogue number: ESF291, Generon) supplemented with 10% Fetal Bovine Serum (FBS), and 1% Penicillin-Streptomycin-Glutamine mix (P/S/G, Invitrogen) at 27ºC. RNAi constructs for UPF1 were amplified by PCR using primers for the desired sequence in addition to the T7 promoter sequence at their 5' end (bold) (5'-**TTAATACGACTCACTATAG**GGGAGA-3'). The PCR product was purified using the Monarch PCR and DNA cleanup kit (T1030S, NEB) and dsRNA was synthesised using the T7 RiboMAX express system (P1700, Promega). In a 6-well plate, 10^6 cells were seeded in each well, incubated overnight, and then treated with 15 µg of dsRNA per well, in serum-free media. The cells are incubated for 1 hour at room temperature before being supplemented with 2 mL of complete media. The cells were incubated for three days to knockdown the UPF1 mRNA, before being harvested. For immunostaining, S2 cells (1 mL corresponding to about 10^6 cells) were seeded onto Concanavalin-A (500 µg/mL) treated coverslips, in a 6-well plate for 30 minutes at 27ºC to allow attachment. Excess media was eluted off and replaced with serum-free media containing typically 250 nM MitoSpy™ Red CMXRos (424801, BioLegend)(in some experiments MitoTracker was used instead, as indicated in the figure legends; MitoTracker™ Red CMXRos, M7512, ThermoFisher Scientific). The cells were incubated with MitoSpy for 30 minutes at 27 ºC, protected from light. Cells were then washed twice in serum-free media, fixed for 15 minutes in 4% paraformaldehyde at room temperature, washed twice in 1X PBS (13 mM NaCl, 0.7 mM Na_2HPO_4, pH 7.4), permeabilised for 15 minutes at room temperature in 0.1% PBT (1X PBS, 0.1% Triton X-100), and blocked for 1 hour at room temperature in blocking solution (5% Bovine Serum Albumin (BSA), 0.05% sodium azide, and 1X PBS). They were then incubated in primary antibody for 16 hours at 4ºC, washed and incubated in the appropriate, fluorophore-conjugated secondary antibody for 2 hours at room temperature. After incubation with antibodies, samples were washed in 1X PBS and incubated with DAPI (4-6-diamidino-2-phenylindole, Sigma-Aldrich, 1 µg/mL) for 10 minutes at room temperature. Samples were briefly washed in 1X PBS and mounted in VectaShield® antifade mounting medium (Vector Laboratories).

Drosophila stocks and husbandry

Flies were reared on standard cornmeal fly food media at 25ºC. The *y* w^{118} strain was used as wild type (DGGR_108736). The following lines were obtained from Bloomington *Drosophila* stock centre: *UAS-GFP-Upf1* (24623), *UAS-Upf1*^{HMC05537} (referred to as UPF1$^{RNAi(1)}$; 43144), *UAS-Upf1*^{GL01485} (referred to as UPF1$^{RNAi(2)}$; 64519), *UAS-mCherry-mito* (66533), *UAS-Upf2*^{JF01560} (31095), *UAS-Upf3*^{HMJ22158} (58181), and *UAS-dj-GFP* (5417). The following *Gal4* drivers *forkhead* (*Fkh)*(Henderson and Andrew, 2000), *myosin heavy chain* (*Mhc*)(Schuster et al., 1996), *bag-of-marbles* (*Bam*)(White-Cooper, 2012), drove expression of UAS constructs within the salivary glands, muscles, and late spermatogonia/early spermatocytes, respectively. *BAC-TFAM-GFP* is controlled by the endogenous promoter within a BAC clone derived transgene (Zhang et al., 2016) and *ubi-mCherry-mito* is a transgenes controlled by the Ubiquitin promoter (Lee et al., 1988).

Combination stocks of second and third chromosomal transgenes were generated through standard combination crosses with a double balancer line (*w; IF/CyO-Act>GFP; MKRS/Tm6, Tb)*.

Antibodies

Antibodies used for immunostaining: rabbit anti-COX4 (COX4I1, NB110-39115, Bio-Techne, diluted 1:100). The anti-UPF1 antibodies used was typically 7B12 or in some instances 1C13 (diluted 1:100). The same anti-UPF1 antibodies were used in ChIP-seq as described previously, Singh et al., 2019.

S2 Cell Fractionation and Western Blotting

To isolate the nuclear and cytoplasmic fractions, 2×10^6 S2 cells were harvested and washed twice with ice-cold 1X PBS. Cells were resuspended in 1 mL ice-cold buffer AT (15 mM HEPES pH 7.6, 10 mM KCl, 5 mM MgOAc, 3 mM $CaCl_2$, 300 mM Sucrose, 0.1% Triton X-100, 1 mM DTT, 1X PhosSTOP (4906845001, Roche), 1X cOmplete, Mini, EDTA-free Protease Inhibitor Cocktail (04693159001, Roche) and 1 U/mL Ribolock RNase Inhibitor) and incubated on ice for 10 min as a hypotonic treatment. Cells were lysed using a 2 mL Dounce homogenizer by applying 30-40 strokes with the tight pestle at 4°C. Lysates were divided into two aliquots of 500 µL and each aliquot was layered over 1 mL cushion of buffer B (15 mM HEPES-KOH at pH 7.6, 10 mM KCl, 5 mM MgOAc, 3 mM $CaCl_2$, 1 M sucrose, 1 mM DTT,

1X cOmplete, Mini, EDTA-free Protease Inhibitor Cocktail). Following the centrifugation at 8000 RPM for 15 min at 4°C, the top layer (300 µL) was collected as cytoplasmic fraction. The pellet was resuspended in 500 µL AT buffer and layered over again on buffer B. Following the centrifugation, the pellet was collected as nuclear fraction. Proteins fractions were analysed by standard western blotting.

Adult and Larval Tissue Immunostaining

Internal organs of third instar larvae were dissected in 1X PBS (13mM NaCl, 0.7 mM Na_2HPO_4, pH 7.4), fixed for 20 minutes at room temperature in 4% paraformaldehyde (methanol-free; 43368.9L, VMR international), washed twice in 1X PBS, and permeabilised in 0.1% PBT (1X PBS, 0.1% Triton X-100). Samples were incubated in blocking solution for 2 hours at room temperature, antibody incubation, and sample mounting remain the same as mentioned above.

Testes of 2–5-day old adult males were dissected in 1X PBS. The only notable changes compared to larval tissue was a fixation time of 30 minutes at room temperature on a rocker, and one hour permeabilization following fixation in 0.3% PBT (1X PBS, 0.3% Triton X-100) at room temperature. All other steps remained the same as mentioned prior. Testes squash preparations were prepared as described previously (Singh and Lakhotia, 2024)

Female muscle dissection followed a previously established protocol (Tenenbaum and Gavis, 2016), the samples were mounted in the same mounting media as mentioned for the prior cell and tissue samples.

Confocal imaging and image analysis

The images of developing spermatids and nebenkern structure were captured under the phase contrast microscopic setting using x63, 1.4-NA oil immersion objective of Nikon Eclipse 80i fluorescence microscope. Confocal z-stack images of mounted samples were acquired using the Zeiss LSM900 with AiryScan2 module, Zeiss LSM710, Leica TCS SP8 STED, and Leica TCS SP2-AOBS confocal microscopes using Plan-Apo 10X, 25X, 63X, 1.4-NA objectives. All objectives, except for 10X, were oil immersion. Images were processed and quantified using FIJI (Schindelin et al., 2012).

Quantification of Total Corrected Fluorescence (TCF) was calculated using FIJI (Schindelin et al., 2012). A mean intensity projection of multi-z-stack image was generated, a region of interest was defined, and then the measure function was used. This was repeated for a background region to identify the mean of background fluorescence (MBF). The output was inserted into the following formula: TCF = Integrated Density – (Area * MBF).

ChIP-seq

Chromatin immunoprecipitation (ChIP) experiments were performed as previously described, (Singh et al., 2019). Briefly, S2 cells (2 x 10^7) were washed and fixed in 1% formaldehyde (EM grade, Polyscience) for 10 minutes at room temperature. Cross-linking was stopped by addition of 125 mM Glycine for 5 minutes at room temperature. Cells were briefly centrifuged at 4ºC, and rinsed in 1X PBS containing 1X cOmplete, Mini, EDTA-free Protease Inhibitor Cocktail. The pellet is resuspended in lysis buffer (5 mM PIPES pH 8.0, 85 mM KCl, 0.5% NP-40) supplemented within the same protease inhibitor cocktail and 1X PhosSTOP. Cells were centrifuged again, and rediluted in nuclear lysis buffer (50 mM Tris pH 8.0, 10 mM EDTA, 1.0% SDS) with protease inhibitor cocktail and PhosSTOP. The cell suspension is diluted with IP dilution buffer (16.7 mM Tris pH 8.0, 1.2 mM EDTA, 167 mM NaCl, 1.1% Triton X-100, 0.01% SDS). They were sonicated for 5 cycles 30s ON/OFF in a Bioruptor sonicator (Diagenode). Samples were centrifuged; clear supernatant is transferred to a 15 mL tube. Aliquot of supernatant was kept for input DNA extraction. Supernatant diluted with IP dilution buffer. Antibody was added to supernatant and incubated overnight on a rocker at 4ºC. Pre-washed DynaBeads were added to the mix and incubated for 1 hour at 4ºC on a rocker. Beads were washed with low salt buffer (0.1% SDS, 1% Triton X-100, 2 mM EDTA, 20mM Tris pH 8.0, 150 mM NaCl), high salt buffer (0.1% SDS, 1% Triton X-100, 2 mM EDTA, 20 mM Tris pH 8.0, 500 mM NaCl) and 1X TE buffer (10 mM Tris pH 8.0, 1 mM EDTA). Beads are then incubated with elution buffer (0.1 M $NaHCO_3$, 1% SDS) at room temperature for 15 minutes and eluted chromatin was reverse cross-linked by adding de-crosslinking buffer (2 M NaCl, 0.1 M EDTA, 0.4M Tris pH 7.5), and incubated at 65ºC overnight on a rotator. Proteinase K (50 mg/mL) was used to digest proteins, for 2 hours at 50ºC on a rocker. DNA was isolated with a Monarch PCR and DNA Cleanup kit. Sequencing and library prep information was previously described (Singh et al., 2019).

ChIP-seq analysis

UPF1 and Ser2 RNA Polymerase II ChIP-seq datasets (GEO: GSE116806) were initially analysed as previously described (Singh et al., 2019). Additional analysis was done with Polymerase II ChIP-seq public datasets (Nechaev et al., 2010)(GEO:GSE18643). Files were trimmed using TRIMMOMATIC (v0.39)(Bolger et al., 2014) to remove low quality reads, and adapter sequences. Output files were aligned to the genome using Bowtie2 v2.5.1 after the construction of a Bowtie2 index of *D. melanogaster* genome BDGP6.46 (Ensembl release 111). The aligned SAM files were converted to BAM files which were sorted and indexed using SAMtools v1.19.2. BAM files were converted to BEDgraph files for visualisation in the genome browser IGV (Robinson et al., 2023) using the command genomeCoverageBed command and the options -bga and -ibam from the deepTools v3.5.2 suite (Ramirez et al., 2014).

Genomic DNA extraction and quantification

In all instances of genomic DNA (gDNA) extraction, the GeneJET Genomic DNA Purification Kit (K0721, ThermoFisher Scientific) was used. For tissue samples, 20 samples were dissected in triplicate in 1X PBS, centrifuged briefly and PBS eluted off. S2 cells (2×10^7) were centrifuged to form a pellet and washed twice, briefly with 1X PBS. Following the centrifugation and removal of the supernatant from samples, extraction was performed using the protocol recommended for: Mammalian Tissue and Rodent Tail Genomic DNA Purification Protocol. Tissue samples were homogenised with pestles after pelleting to the bottom of the tube by centrifugation, whilst S2 cells were resuspended in the kit-provided digestion solution, directly. A minimum of two hours was allowed for digestion of the sample, testes samples required a longer incubation of 5 hours for complete dissolution. At this point DNA was purified as described in the kit protocol.

To assess mtDNA copy number, extracted gDNA was diluted 1:50 in nuclease-free dH_2O, prior to addition to the qPCR reaction. Each reaction consisted of 3 µL of a primer mix (final concentration of 400 nM), 2 µL of diluted gDNA and 5 µL qPCRBIO SyGreen Blue Mix Hi-ROX (PB20.16-50, PCR Biosystems Ltd).

RNA extraction and quantification and sequencing

Testes were dissected in 1X PBS, and transferred into ice-cold 1X PBS, the tissue was centrifuged at 1000 g for 30 seconds, the supernatant eluted off, and directly resuspended in 1 mL TRIzol™ Reagent (15596029, ThermoFisher Scientific). Tissue was incubated for 15 minutes at room temperature, vortexed for 1 minute, and 200 µL chloroform was added. Tubes were inverted by hand for 15 seconds until there was a homogenous suspension. Samples were centrifuged for 20 minutes at 15 000 g at 4ºC. The top aqueous phase was eluted and collected in a sterile microcentrifuge tube. 1 µL RNase-free molecular grade glycogen (10901393001, Merck), and an equal amount ice-cold isopropanol was added. Samples were incubated on ice for 20 minutes to allow precipitation of RNA and centrifuged for 20 minutes at 15 000 g. The supernatant was discarded, and the pellet was washed twice in 75% ethanol, with 5-minute centrifuge spins. The pellet is allowed to dry and is resuspended in 20 µL DEPC-treated water. Quality and quantification of RNA following dissolution was assessed and concentration measured using a spectrophotometer (Nanodrop-8000, ND-8000-GL, ThermoFisher Scientific). Quantification of RNA targets was assessed by RT-qPCR. Synthesis of cDNA used the qScript cDNA synthesis kit (7331174, QuantaBio), 200 ng of RNA was added to the 1X master mix alongside 1X qScript reverse transcriptase and the final volume was adjusted to 20 µL with the addition of nuclease-free water. Samples were placed in a thermocycler for the following steps: 22ºC for 5 minutes, 42ºC for 1 hour, and 82ºC for 5 minutes. The product of cDNA synthesis was diluted 1:25 in nuclease-free water and proceeded with RT-qPCR quantification. The same reaction was prepared as for gDNA quantification, mentioned prior (primer concentration was 400 nM).

RNA-sequencing and analysis

Prior to sequencing, PolyA mRNA was enriched. RNA libraries were then prepared commercially by Novogene, and commercially assessed for quality. Sequencing of RNA was paired end of 150 bp in length and sequenced on Illumina NovaSeq platforms.

FASTQ files (GEO: GSE266138) were trimmed using TRIMMOMATIC PE (v0.39) (Bolger et al., 2014). Once trimmed, files were aligned to the *D. melanogaster* genome (BDGP6.56, FlyBase release FB2024_01), using HISAT2 (v2.2.1), after the construction of an HISAT2 index with the build function (Kim et al., 2019). SAMtools (v1.19.2) was used to convert the SAM files and to sort the BAM files based on genomic coordinates (Li et al., 2009). Read

counts were extracted using HTSeq count function (v0.13.5)(Anders et al., 2015), and differential expression analysis was conducted using DESeq2 in R (Love et al., 2014).

Primer list

UPF1: F 5′-CCAGCATCACCAACGATCTG-3′, R 5′-AGTTGTTGCACATGACCACC-3

UPF2: F 5′-TCAAGGCCACCGAGAAGATT-3′, R 5′-AATGCACCAGAACAACACCC-3′

UPF3: F 5′-CTCCCTTCCAGTGCTTCCTT-3′, R 5′-GGAGGGGTGTAGACTTGACC-3′

RpL32: F: 5′-CTCCCTTCCAGTGCTTCCTT-3′, R: 5′-GGAGGGGTGTAGACTTGACC-3′

Cox1: F 5′-TCCTGATATAGCATTCCCACGA-3′, R 5′-CCACCATGAGCAATTCCAGC-3′

ND4: F 5′-GCTCATGTTGAAGCTCCAGT-3′, R 5′-AAGCCTTTAAATCAGTTTGACGT-3′

Cyt-b: F 5′-CACCTGCCCATATTCAACCAGAATG-3′, R 5′-CAACTGGTCGAGCTCCAATTCAAG-3′

16S lrRNA: F 5′-AGTCTAACCTGCCCACTGAA-3′, R 5′-TCCAACCATTCATTCCAGCC-3′

TFAM: F 5′-CCCAGATTACCACCGTCGAG-3′, R 5′-TTGTTGGTCCCGCTTGAACT-3′

Acknowledgments

We would like to thank the following for fly lines provided for this study. Helen White-Cooper (University of Cardiff) for sending us *BamGAL4:VP16*, Alicia Hidalgo (University of Birmingham) for providing us the *MhcGAL4* line for adult muscle experiments, and Hansong Ma (University of Birmingham) for providing, *Dj-GFP*, *BAC-TFAM-GFP*, and the unpublished *ubi-mito-mCherry* line. The authors are also grateful to the staff of the Birmingham Advanced Light Microscopy (BALM) facilities, at the University of Birmingham. Also, the STED super-resolution microscopy of SATHI-Central Discovery Centre, and Confocal microscopy and advanced light microscopy (Interdisciplinary school of Life Sciences, Institute of Sciences, Banaras Hindu University, India) facilities. We would also like to thank the Biological Sciences Research Council [BBSRC BB/S017984/1, and The Midlands Integrative Biosciences (Doctoral) Training Partnership (MIBTP) studentship to HLD] for funding this research.

References

ALTAMURA, N., GROUDINSKY, O., DUJARDIN, G. & SLONIMSKI, P. P. 1992. Nam7 nuclear gene encodes a novel member of a family of helicases with a Zn-ligand motif and is involved in mitochondrial functions in *Saccharomyces cerevisiae*. *Journal of Molecular Biology,* 224**,** 575-587.

ANDERS, S., PYL, P. T. & HUBER, W. 2015. HTSeq--a Python framework to work with high-throughput sequencing data. *Bioinformatics,* 31**,** 166-9.

ASHER, E. B., GROUDINSKY, O., DUJARDIN, G., ALTAMURA, N., KERMORGANT, M. & SLONIMSKI, P. P. 1989. Novel class of nuclear genes involved in both mRNA splicing and protein synthesis in Saccharomyces cerevisiae mitochondria. *Mol Gen Genet,* 215**,** 517-28.

BADER, G., ENKLER, L., ARAISO, Y., HEMMERLE, M., BINKO, K., BARANOWSKA, E., DE CRAENE, J. O., RUER-LAVENTIE, J., PIETERS, J., TRIBOUILLARD-TANVIER, D., SENGER, B., DI RAGO, J. P., FRIANT, S., KUCHARCZYK, R. & BECKER, H. D. 2020. Assigning mitochondrial localization of dual localized proteins using a yeast Bi-Genomic Mitochondrial-Split-GFP. *Elife,* 9.

BAO, J. Q., VITTING-SEERUP, K., WAAGE, J., TANG, C., GE, Y., PORSE, B. T. & YAN, W. 2016. UPF2-Dependent Nonsense-Mediated mRNA Decay Pathway Is Essential for Spermatogenesis by Selectively Eliminating Longer 3′ UTR Transcripts. *Plos Genetics,* 12.

BHATTACHARYA, A., CZAPLINSKI, K., TRIFILLIS, P., HE, F., JACOBSON, A. & PELTZ, S. W. 2000. Characterization of the biochemical properties of the human Upf1 gene product that is involved in nonsense-mediated mRNA decay. *RNA,* 6**,** 1226-35.

BOGENHAGEN, D. F. 2012. Mitochondrial DNA nucleoid structure. *Biochimica Et Biophysica Acta-Gene Regulatory Mechanisms,* 1819**,** 914-920.

BOLGER, A. M., LOHSE, M. & USADEL, B. 2014. Trimmomatic: a flexible trimmer for Illumina sequence data. *Bioinformatics,* 30**,** 2114-20.

BROGNA, S., MCLEOD, T. & PETRIC, M. 2016. The Meaning of NMD: Translate or Perish. *Trends Genet,* 32**,** 395-407.

BROGNA, S. & WEN, J. 2009. Nonsense-mediated mRNA decay (NMD) mechanisms. *Nat Struct Mol Biol,* 16**,** 107-13.

BYKOV, Y. S., FLOHR, T., BOOS, F., ZUNG, N., HERRMANN, J. M. & SCHULDINER, M. 2022. Widespread use of unconventional targeting signals in mitochondrial ribosome proteins. *Embo Journal,* 41.

CHACINSKA, A., KOEHLER, C. M., MILENKOVIC, D., LITHGOW, T. & PFANNER, N. 2009. Importing Mitochondrial Proteins: Machineries and Mechanisms. *Cell,* 138**,** 628-644.

CHAKRABARTI, S., JAYACHANDRAN, U., BONNEAU, F., FIORINI, F., BASQUIN, C., DOMCKE, S., LE HIR, H. & CONTI, E. 2011. Molecular mechanisms for the RNA-dependent ATPase activity of Upf1 and its regulation by Upf2. *Mol Cell,* 41**,** 693-703.

CHEN, H., MA, J., KONG, F., SONG, N., WANG, C. & MA, X. 2022. UPF1 contributes to the maintenance of endometrial cancer stem cell phenotype by stabilizing LINC00963. *Cell Death Dis,* 13**,** 257.

CULBERTSON, M. R. 1999. RNA surveillance - unforeseen consequences for gene expression, inherited genetic disorders and cancer. *Trends in Genetics,* 15**,** 74-80.

CZAPLINSKI, K., WENG, Y., HAGAN, K. W. & PELTZ, S. W. 1995. Purification and characterization of the Upf1 protein - a factor involved in translation and messenger RNA degradation. *RNA,* 1**,** 610-623.

DE PINTO, B., LIPPOLIS, R., CASTALDO, R. & ALTAMURA, N. 2004. Overexpression of Upf1p compensates for mitochondrial splicing deficiency independently of its role in mRNA surveillance. *Mol Microbiol,* 51**,** 1129-42.

DE, S., EDWARDS, D. M., DWIVEDI, V., WANG, J., VARSALLY, W., DIXON, H. L., SINGH, A. K., OWUAMALAM, P. O., WRIGHT, M. T., SUMMERS, R. P., HOSSAIN, M. N., PRICE, E. M., WOJEWODZIC, M. W., FALCIANI, F., HODGES, N. J., SAPONARO, M., TANAKA, K., AZZALIN, C. M., BAUMANN, P., HEBENSTREIT, D. & BROGNA, S. 2022. Genome-wide chromosomal association of Upf1 is linked to Pol II transcription in Schizosaccharomyces pombe. *Nucleic Acids Res,* 50**,** 350-367.

DELUCA, S. Z. & O'FARRELL, P. H. 2012. Barriers to male transmission of mitochondrial DNA in sperm development. *Dev Cell,* 22**,** 660-8.

DOROGOVA, N. V., BOLOBOLOVA, E. U., AKHMETOVA, K. A. & FEDOROVA, S. A. 2013. Drosophila male-sterile mutation emmenthal specifically affects the mitochondrial morphogenesis. *Protoplasma,* 250**,** 515-20.

FABIAN, L. & BRILL, J. A. 2012. Drosophila spermiogenesis: Big things come from little packages. *Spermatogenesis,* 2**,** 197-212.

FANOURGAKIS, G., LESCHE, M., AKPINAR, M., DAHL, A. & JESSBERGER, R. 2016. Chromatoid Body Protein TDRD6 Supports Long 3′ UTR Triggered Nonsense Mediated mRNA Decay. *Plos Genetics,* 12.

FATSCHER, T., BOEHM, V. & GEHRING, N. H. 2015. Mechanism, factors, and physiological role of nonsense-mediated mRNA decay. *Cell Mol Life Sci,* 72**,** 4523-44.

FIORINI, F., BAGCHI, D., LE HIR, H. & CROQUETTE, V. 2015. Human Upf1 is a highly processive RNA helicase and translocase with RNP remodelling activities. *Nat Commun,* 6**,** 7581.

FUKASAWA, Y., TSUJI, J., FU, S. C., TOMII, K., HORTON, P. & IMAI, K. 2015. MitoFates: Improved Prediction of Mitochondrial Targeting Sequences and Their Cleavage Sites. *Molecular & Cellular Proteomics,* 14**,** 1113-1126.

GIANSANTI, M. G. & FULLER, M. T. 2012. What Drosophila spermatocytes tell us about the mechanisms underlying cytokinesis. *Cytoskeleton (Hoboken),* 69**,** 869-81.

GIANSANTI, M. G., SECHI, S., FRAPPAOLO, A., BELLONI, G. & PIERGENTILI, R. 2012. Cytokinesis in Drosophila male meiosis. *Spermatogenesis,* 2**,** 185-196.

GOETZ, A. E. & WILKINSON, M. 2017. Stress and the nonsense-mediated RNA decay pathway. *Cell Mol Life Sci,* 74**,** 3509-3531.

HALES, K. G. & FULLER, M. T. 1997. Developmentally regulated mitochondrial fusion mediated by a conserved, novel, predicted GTPase. *Cell,* 90**,** 121-9.

HAN, X., WEI, Y. L., WANG, H., WANG, F. L., JU, Z. Y. & LI, T. L. 2018. Nonsense-mediated mRNA decay: a 'nonsense' pathway makes sense in stem cell biology. *Nucleic Acids Research,* 46**,** 1038-1051.

HE, F. & JACOBSON, A. 2015. Nonsense-Mediated mRNA Decay: Degradation of Defective Transcripts Is Only Part of the Story. *Annu Rev Genet.*

HENDERSON, K. D. & ANDREW, D. J. 2000. Regulation and function of Scr, exd, and hth in the Drosophila salivary gland. *Dev Biol,* 217**,** 362-74.

HOGG, J. R. & GOFF, S. P. 2010. Upf1 senses 3'UTR length to potentiate mRNA decay. *Cell,* 143**,** 379-89.

HOLT, I. J. & REYES, A. 2012. Human mitochondrial DNA replication. *Cold Spring Harb Perspect Biol,* 4.

HUG, N., LONGMAN, D. & CACERES, J. F. 2016. Mechanism and regulation of the nonsense-mediated decay pathway. *Nucleic Acids Res,* 44**,** 1483-95.

HURT, J. A., ROBERTSON, A. D. & BURGE, C. B. 2013. Global analyses of UPF1 binding and function reveal expanded scope of nonsense-mediated mRNA decay. *Genome Res,* 23**,** 1636-50.

JOERS, P. & JACOBS, H. T. 2013. Analysis of replication intermediates indicates that Drosophila melanogaster mitochondrial DNA replicates by a strand-coupled theta mechanism. *PLoS One,* 8**,** e53249.

KAROUSIS, E. D., NASIF, S. & MUHLEMANN, O. 2016. Nonsense-mediated mRNA decay: novel mechanistic insights and biological impact. *Wiley Interdiscip Rev RNA,* 7**,** 661-82.

KAUFMAN, B. A., DURISIC, N., MATIVETSKY, J. M., COSTANTINO, S., HANCOCK, M. A., GRUTTER, P. & SHOUBRIDGE, E. A. 2007. The mitochondrial transcription factor TFAM coordinates the assembly of multiple DNA molecules into nucleoid-like structures. *Molecular Biology of the Cell,* 18**,** 3225-3236.

KIM, D., PAGGI, J. M., PARK, C., BENNETT, C. & SALZBERG, S. L. 2019. Graph-based genome alignment and genotyping with HISAT2 and HISAT-genotype. *Nat Biotechnol,* 37**,** 907-915.

KIM, J., KIM, H. S. & CHUNG, J. H. 2023. Molecular mechanisms of mitochondrial DNA release and activation of the cGAS-STING pathway. *Experimental and Molecular Medicine,* 55**,** 510-519.

KIM, Y. K. & MAQUAT, L. E. 2019. UPFront and center in RNA decay: UPF1 in nonsense-mediated mRNA decay and beyond. *RNA,* 25**,** 407-422.

KUKAT, C., DAVIES, K. M., WURM, C. A., SPAHR, H., BONEKAMP, N. A., KUHL, I., JOOS, F., POLOSA, P. L., PARK, C. B., POSSE, V., FALKENBERG, M., JAKOBS, S., KUHLBRANDT, W. & LARSSON, N. G. 2015. Cross-strand binding of TFAM to a single mtDNA molecule forms the mitochondrial nucleoid. *Proc Natl Acad Sci U S A,* 112**,** 11288-93.

LEE, H. S., SIMON, J. A. & LIS, J. T. 1988. Structure and Expression of Ubiquitin Genes of Drosophila-Melanogaster. *Molecular and Cellular Biology,* 8**,** 4727-4735.

LEE, W., ZAMUDIO-OCHOA, A., BUCHEL, G., PODLESNIY, P., MARTI GUTIERREZ, N., PUIGROS, M., CALDERON, A., TANG, H. Y., LI, L., MIKHALCHENKO, A., KOSKI, A., TRULLAS, R., MITALIPOV, S. & TEMIAKOV, D. 2023. Molecular basis for maternal inheritance of human mitochondrial DNA. *Nat Genet,* 55**,** 1632-1639.

LEEDS, P., PELTZ, S. W., JACOBSON, A. & CULBERTSON, M. R. 1991. The product of the yeast Upf1 gene is required for rapid turnover of messenger RNAs containing a premature translational termination codon. *Genes & development,* 5**,** 2303-2314.

LEHTINIEMI, T., BOURGERY, M., MA, L., AHMEDANI, A., MÄKELÄ, M., ASTELJOKI, J., OLOTU, O., LAASANEN, S., ZHANG, F. P., TAN, K., CHOUSAL, J. N., BUROW, D., KOSKINEN, S., LAIHO, A., ELO, L. L., CHALMEL, F., WILKINSON, M. F. & KOTAJA, N. 2022. SMG6 localizes to the chromatoid body and shapes the male germ cell transcriptome to drive spermatogenesis. *Nucleic Acids Research,* 50**,** 11470-11491.

LEWIS, D. L., FARR, C. L., FARQUHAR, A. L. & KAGUNI, L. S. 1994. Sequence, Organization, and Evolution of the a+T Region of Drosophila-Melanogaster Mitochondrial-DNA. *Molecular Biology and Evolution,* 11**,** 523-538.

LI, A. Y. Z., DI, Y., RATHORE, S., CHIANG, A. C., JEZEK, J. & MA, H. 2023. Milton assembles large mitochondrial clusters, mitoballs, to sustain spermatogenesis. *Proc Natl Acad Sci U S A,* 120**,** e2306073120.

LI, H., HANDSAKER, B., WYSOKER, A., FENNELL, T., RUAN, J., HOMER, N., MARTH, G., ABECASIS, G., DURBIN, R. & GENOME PROJECT DATA

PROCESSING, S. 2009. The Sequence Alignment/Map format and SAMtools. *Bioinformatics,* 25**,** 2078-9.
LOVE, M. I., HUBER, W. & ANDERS, S. 2014. Moderated estimation of fold change and dispersion for RNA-seq data with DESeq2. *Genome Biol,* 15**,** 550.
LYKKE-ANDERSEN, S. & JENSEN, T. H. 2015. Nonsense-mediated mRNA decay: an intricate machinery that shapes transcriptomes. *Nat Rev Mol Cell Biol,* 16**,** 665-77.
NECHAEV, S., FARGO, D. C., DOS SANTOS, G., LIU, L. W., GAO, Y. & ADELMAN, K. 2010. Global Analysis of Short RNAs Reveals Widespread Promoter-Proximal Stalling and Arrest of Pol II in. *Science,* 327**,** 335-338.
NOGUCHI, T., KOIZUMI, M. & HAYASHI, S. 2011. Sustained elongation of sperm tail promoted by local remodeling of giant mitochondria in Drosophila. *Curr Biol,* 21**,** 805-14.
PATEL, M. R. 2017. Inheritance: Male mtDNA Just Can't Catch a Break. *Curr Biol,* 27**,** R264-R266.
RAMIREZ, F., DUNDAR, F., DIEHL, S., GRUNING, B. A. & MANKE, T. 2014. deepTools: a flexible platform for exploring deep-sequencing data. *Nucleic Acids Res,* 42**,** W187-91.
RILEY, J. S. & TAIT, S. W. 2020. Mitochondrial DNA in inflammation and immunity. *EMBO Rep,* 21**,** e49799.
ROBINSON, J. T., THORVALDSDOTTIR, H., TURNER, D. & MESIROV, J. P. 2023. igv.js: an embeddable JavaScript implementation of the Integrative Genomics Viewer (IGV). *Bioinformatics,* 39.
SANTEL, A., WINHAUER, T., BLUMER, N. & RENKAWITZ-POHL, R. 1997. The Drosophila don juan (dj) gene encodes a novel sperm specific protein component characterized by an unusual domain of a repetitive amino acid motif. *Mech Dev,* 64**,** 19-30.
SAVOJARDO, C., BRUCIAFERRI, N., TARTARI, G., MARTELLI, P. L. & CASADIO, R. 2020. DeepMito: accurate prediction of protein sub-mitochondrial localization using convolutional neural networks. *Bioinformatics,* 36**,** 56-64.
SCHINDELIN, J., ARGANDA-CARRERAS, I., FRISE, E., KAYNIG, V., LONGAIR, M., PIETZSCH, T., PREIBISCH, S., RUEDEN, C., SAALFELD, S., SCHMID, B., TINEVEZ, J. Y., WHITE, D. J., HARTENSTEIN, V., ELICEIRI, K., TOMANCAK, P. & CARDONA, A. 2012. Fiji: an open-source platform for biological-image analysis. *Nat Methods,* 9**,** 676-82.
SCHUSTER, C. M., DAVIS, G. W., FETTER, R. D. & GOODMAN, C. S. 1996. Genetic dissection of structural and functional components of synaptic plasticity. I. Fasciclin II controls synaptic stabilization and growth. *Neuron,* 17**,** 641-54.
SHAMI, G. J., SAMARSKA, I. V., KOEK, G. H., LI, A., PALMA, E., CHOKSHI, S., WISSE, E. & BRAET, F. 2023. Giant mitochondria in human liver disease. *Liver Int,* 43**,** 2365-2378.
SINGH, A. K., CHOUDHURY, S. R., DE, S., ZHANG, J., KISSANE, S., DWIVEDI, V., RAMANATHAN, P., ORSINI, L., HEBENSTREIT, D. & BROGNA, S. 2019. The RNA helicase UPF1 associates with mRNAs co-transcriptionally and is required for the release of mRNAs from transcription sites. *eLife,* 2019;8:e41444.
SINGH, A. K. & LAKHOTIA, S. C. 2024. Visualizing dynamic organization of nuclei and mitochondria during spermatogenesis in Drosophila. *In:* LAKHOTIA, S. C. (ed.) *Experiments with Drosophila for Biology Courses.* 2 ed.: Indian Academy of Sciences Bengaluru.

SINGH, A. K., ZHANG, J., HEBENSTREIT, D. & BROGNA, S. 2020. Evidence of slightly increased Pol II pausing in UPF1-depleted Drosophila melanogaster cells. *MicroPubl Biol,* 2020.

STASZEWSKI, J., LAZAREWICZ, N., KONCZAK, J., MIGDAL, I. & MACIASZCZYK-DZIUBINSKA, E. 2023. UPF1-From mRNA Degradation to Human Disorders. *Cells,* 12.

TENENBAUM, C. M. & GAVIS, E. R. 2016. Removal of Drosophila Muscle Tissue from Larval Fillets for Immunofluorescence Analysis of Sensory Neurons and Epidermal Cells. *J Vis Exp*.

TORRES, T. T., DOLEZAL, M., SCHLOTTERER, C. & OTTENWALDER, B. 2009. Expression profiling of Drosophila mitochondrial genes via deep mRNA sequencing. *Nucleic Acids Res,* 37**,** 7509-18.

WHITE-COOPER, H. 2012. Tissue, cell type and stage-specific ectopic gene expression and RNAi induction in the Drosophila testis. *Spermatogenesis,* 2**,** 11-22.

YU, Z., O'FARRELL, P. H., YAKUBOVICH, N. & DELUCA, S. Z. 2017. The Mitochondrial DNA Polymerase Promotes Elimination of Paternal Mitochondrial Genomes. *Curr Biol,* 27**,** 1033-1039.

ZAEPFEL, B. L., ZHANG, Z., MAULDING, K., COYNE, A. N., CHENG, W., HAYES, L. R., LLOYD, T. E., SUN, S. & ROTHSTEIN, J. D. 2021. UPF1 reduces C9orf72 HRE-induced neurotoxicity in the absence of nonsense-mediated decay dysfunction. *Cell Rep,* 34**,** 108925.

ZHANG, Y., CHEN, Y., GUCEK, M. & XU, H. 2016. The mitochondrial outer membrane protein MDI promotes local protein synthesis and mtDNA replication. *EMBO J,* 35**,** 1045-57.

ZUND, D., GRUBER, A. R., ZAVOLAN, M. & MUHLEMANN, O. 2013. Translation-dependent displacement of UPF1 from coding sequences causes its enrichment in 3' UTRs. *Nat Struct Mol Biol,* 20**,** 936-43.

ZUNIGA, G., LEVY, S., RAMIREZ, P., DE MANGE, J., GONZALEZ, E., GAMEZ, M. & FROST, B. 2023. Tau-induced deficits in nonsense-mediated mRNA decay contribute to neurodegeneration. *Alzheimers Dement,* 19**,** 405-420.

Figures and legends

Figure 1

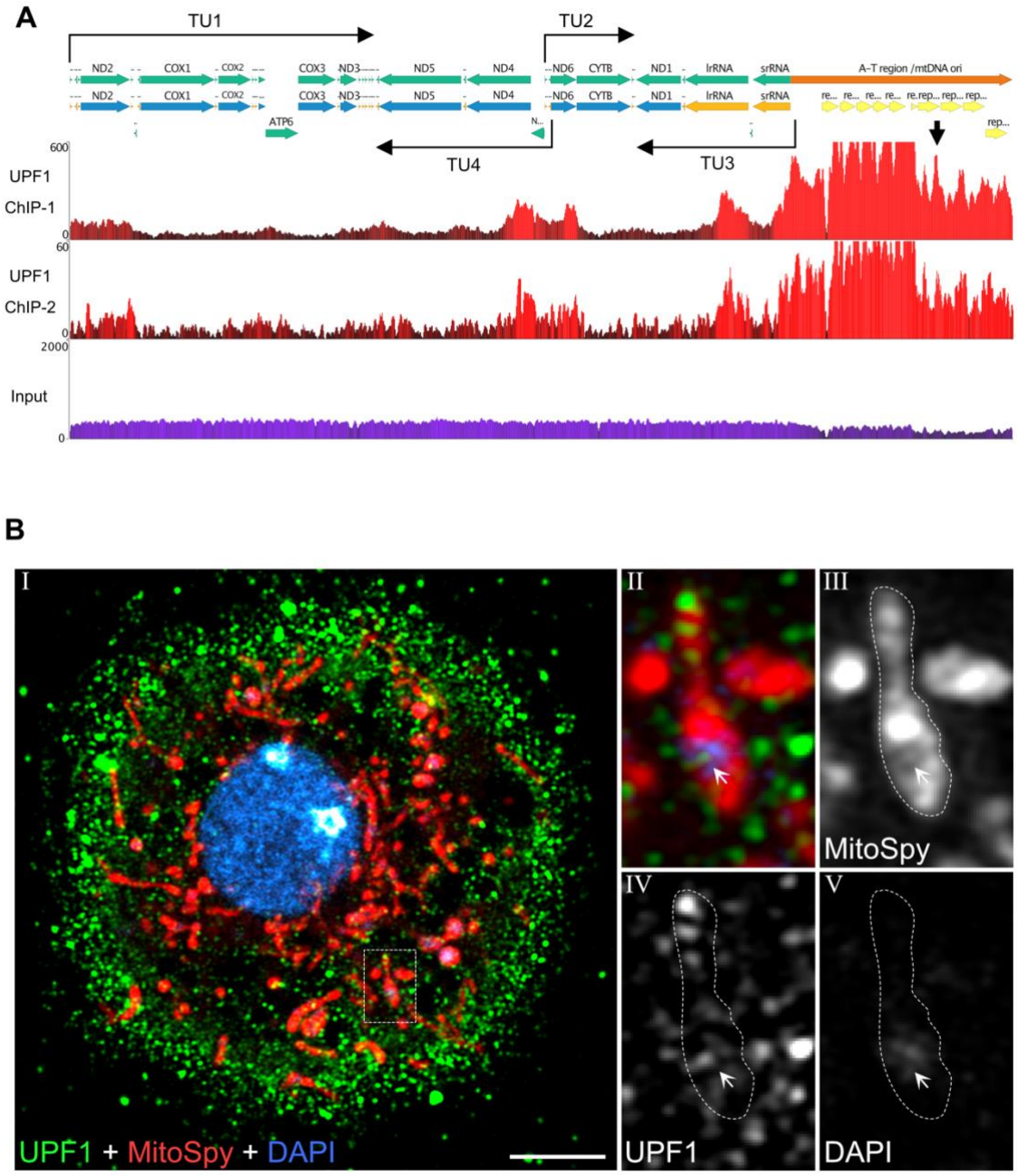

Figure 1. UPF1 mtDNA association and mitochondrial localisation in S2 cells. (**A**) The top panel shows the linear map of the mtDNA and the location of the four transcription start sites and the corresponding transcription units (TUs), TU1 and TU2 on the top strand, TU3 and TU4 on the bottom strand. The protein-coding and rRNA genes are indicated in green, the A-T region / NCR is indicated in orange, blue indicates protein coding genes, orange indicates small and large rRNA, srRNA and lrRNA, respectively, yellow arrows indicate sequence repeats within NCR. The black arrow indicates a prominent peak of enrichment at one of the interrepeat regions. Bottom three panels show genome browsers enrichment profiles of two independent UPF1 ChIP-Seq experiments (red) and, as control, the profile of the input chromatin DNA (purple). The Y axes were not equalised to show that although the two Upf1 samples show different absolute levels of enrichment, the pattern is very similar. (**B**) Fluorescence immunolocalisation of endogenous UPF1 (green) in S2 cells. The red signal corresponds to MitoSpy, a fluorescent dye that localises to the mitochondrial matrix (Materials and Methods). The blue signal corresponds to DAPI, which labels the nuclear DNA and the mtDNA. Panel I shows a merge image in the three channels of a whole cell: magnified views of the boxed region as shown in panels II – V, either as a merged image (panel II) or individual labelled channels in grey. The arrow points to a strong UPF1 signal Dot adjacent to the DAPI stained region of the mitochondria. The images were taken using a Zeiss confocal microscope equipped with a 63X objective lens (Materials and Methods). The scale bar corresponds to 10 µm.

Figure S1

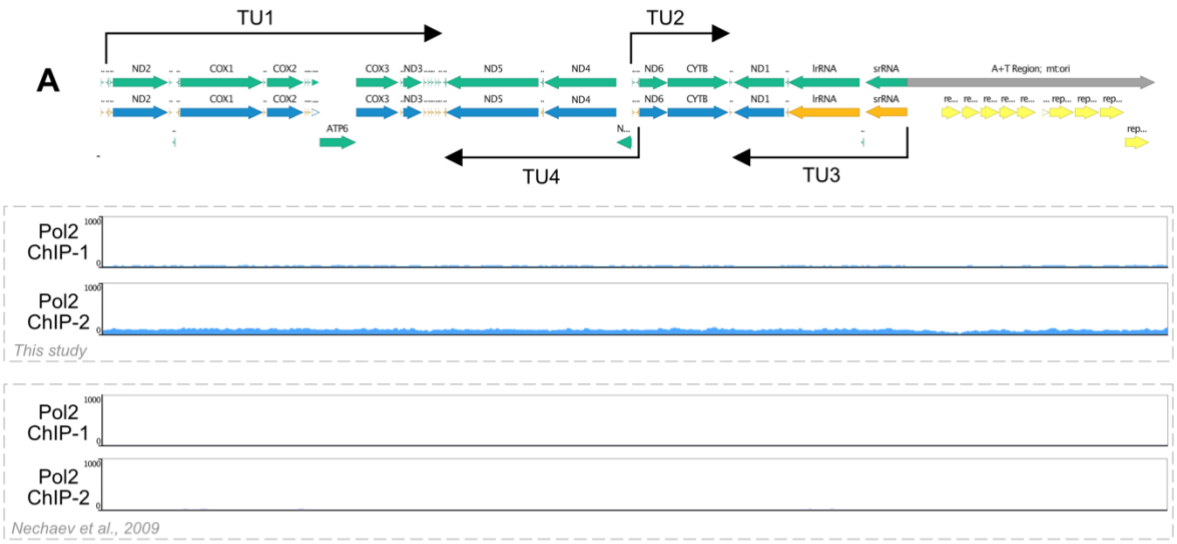
A
TU1
TU2
TU3
TU4
ND2
COX1
COX2
COX3
ND3
ND5
ND4
ND6
CYTB
ND1
lrRNA
srRNA
A+T Region; mt:ori
ATP6
Pol2 ChIP-1
Pol2 ChIP-2
This study
Nechaev et al., 2009

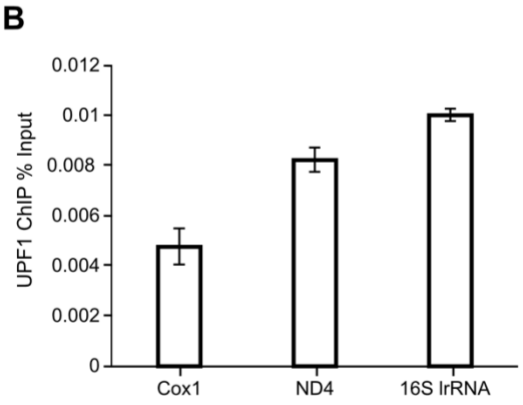
B
UPF1 ChIP % Input
0.012
0.01
0.008
0.006
0.004
0.002
0
Cox1
ND4
16S lrRNA

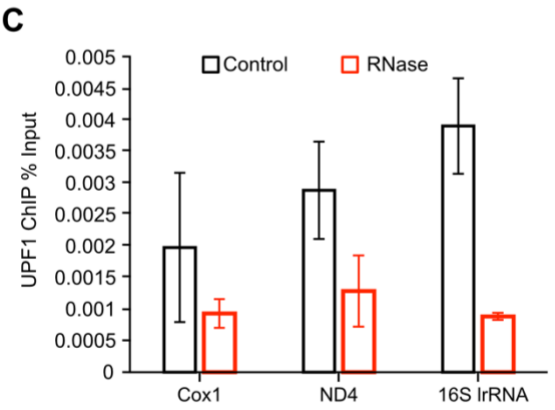
C
Control
RNase
UPF1 ChIP % Input
0.005
0.0045
0.004
0.0035
0.003
0.0025
0.002
0.0015
0.001
0.0005
0
Cox1
ND4
16S lrRNA

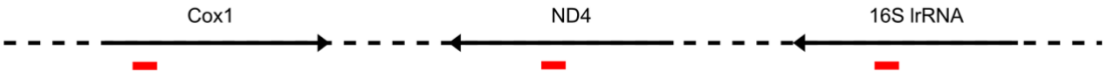
Cox1
ND4
16S lrRNA

Figure S1. ChIP-qPCR validation and RNase sensitivity evidence. (**A**) Top panel shows the annotated linear map of the mitochondrial genome. First two panels below show lack of mtDNA enrichment in two independent Pol II ChIP-Seq experiments (Singh et al., 2020). The next two rows show lack of enrichment in two Pol II ChIP-Seq datasets from a different laboratory (Nechaev et al., 2010). (**B**) ChIP-qPCR examination of UPF1 association with the three mtDNA gene regions indicated, Cox1, ND4 and lrRNA. The location of the three primer pairs are indicated in red in the schematic below. (**C**) UPF1 ChIP-qPCR of the three mtDNA genes with, or without RNase treatment of the chromatin prior the IP (Material and Methods), error bars represent the standard error of the mean. The values are based on two separate ChIP experiments.

Figure S2

A

mtDNA genes *UPF1*^{RNAi} *S2 Cells*

Gene Name	Log2FoldChange	p.value	p.adj
mt:ATPase6	-0.121669908	0.455483759	0.784266753
mt:ATPase8	-1.736109965	0.324959313	NA
mt:CoI	-0.241918765	0.000000179	0.000005985
mt:CoII	-0.288249221	0.000000258	0.000008320
mt:CoIII	-0.202789511	0.000079273	0.001383755
mt:Cyt-b	-0.268682084	0.000000323	0.000010237
mt:ND1	-0.298109754	0.010563206	0.075986127
mt:ND2	-0.555731377	0.546109649	0.841280897
mt:ND3	-0.120528376	0.320077531	0.680294723
mt:ND4	-0.297717782	0.000354183	0.004889467
mt:ND4L	-0.613842504	0.689865305	NA
mt:ND5	-0.268765505	0.000226627	0.003378989
mt:ND6	-0.07744984	0.988707185	0.996907816
mt:lrRNA	-0.089955585	0.029472105	0.163034407
mt:srRNA	-0.954116292	0.282646421	0.640257414

B

mtDNA genes *Fkh>UPF1*$^{RNAi(1)}$

Gene Name	Log2FoldChange	p.value	p.adj
mt:ATPase6	-1.064638193	0.21726853	0.380979979
mt:ATPase8	-2.619035488	0.3360715	NA
mt:CoI	-1.507321801	0.01368995	0.050600251
mt:CoII	-1.421391473	0.0698595	0.170921298
mt:CoIII	-1.548656547	0.01328066	0.04953913
mt:Cyt-b	-1.531484214	0.01529322	0.054928285
mt:ND1	-1.88941363	0.04645774	0.126788606
mt:ND2	-1.661285833	0.03378138	0.099848797
mt:ND3	-1.756886338	0.10512852	0.228219209
mt:ND4	-1.651485544	0.0396875	0.112962419
mt:ND4L	-2.184730294	0.13129804	0.267807009
mt:ND5	-1.291950222	0.04619594	0.126262472
mt:ND6	-1.71356677	NA	NA
mt:lrRNA	-1.689974479	0.01520677	0.054768336
mt:srRNA	-1.913230769	0.11958353	0.250274566

C

mtDNA genes *Fkh>UPF2*^{RNAi}

Gene Name	Log2FoldChange	p.value	p.adj
mt:ATPase6	1.2486244	0.1478475	0.363786545
mt:ATPase8	2.014782085	0.41995207	NA
mt:CoI	-0.182363269	0.76549881	0.891061789
mt:CoII	0.208435539	0.79036004	0.902648397
mt:CoIII	-0.167575538	0.7887446	0.901642718
mt:Cyt-b	0.53358748	0.39807943	0.643397632
mt:ND1	0.355431542	0.70789848	0.862527347
mt:ND2	2.429926173	0.00164331	0.013163756
mt:ND3	0.980146376	0.36585028	0.615786272
mt:ND4	0.605066873	0.45097366	0.689422963
mt:ND4L	3.129284157	0.00275156	0.020088807
mt:ND5	0.948505689	0.14320596	0.356875664
mt:ND6	2.678818176	NA	NA
mt:lrRNA	0.287255186	0.67989716	0.845704147
mt:srRNA	1.498542924	0.22235962	0.46552907

D

mtDNA genes *Fkh>UPF3*^{RNAi}

Gene Name	Log2FoldChange	p.value	p.adj
mt:ATPase6	-0.743827145	0.38865983	0.646657101
mt:ATPase8	-1.611815403	0.55384749	NA
mt:CoI	-0.70531211	0.23104876	0.52161441
mt:CoII	-0.732260899	0.47283655	0.489529618
mt:CoIII	-0.562854103	0.25942911	0.712781192
mt:Cyt-b	-0.602721259	0.33981345	0.601857809
mt:ND1	-1.140490023	0.22932051	0.488270272
mt:ND2	-0.715083437	0.35750747	0.618709769
mt:ND3	-1.010918687	0.35105467	0.612163797
mt:ND4	-0.828623677	0.30197338	0.56648805
mt:ND4L	1.410627975	0.18797572	0.439625122
mt:ND5	-0.468465065	0.4696921	0.709774234
mt:ND6	-0.62618999	NA	NA
mt:lrRNA	-0.264192082	0.70433415	0.864686084
mt:srRNA	-0.171519744	0.88894132	0.956401186

Figure S2. RNA-seq analysis indicates downregulation of mtDNA genes in UPF1KD S2 cells and salivary glands. (**A**) DESeq2 differential expression analysis of mtDNA genes n = 15, values were calculated based on the comparison against 17610 expressed genes, in S2 cells; and 17284 genes in salivary glands (**B-D**). UPF1KD (A and B), UPF2KD (C) and UPF3KD (D). Gene ID, log2FoldChange, P-value (p.value) and the adjusted P-value (p.adj) values are shown. Downregulated and upregulated genes with an associated p.adj value of either <0.05 (A and C) or ≤0.05 (B) are highlighted in green and red, respectively.

Figure S3

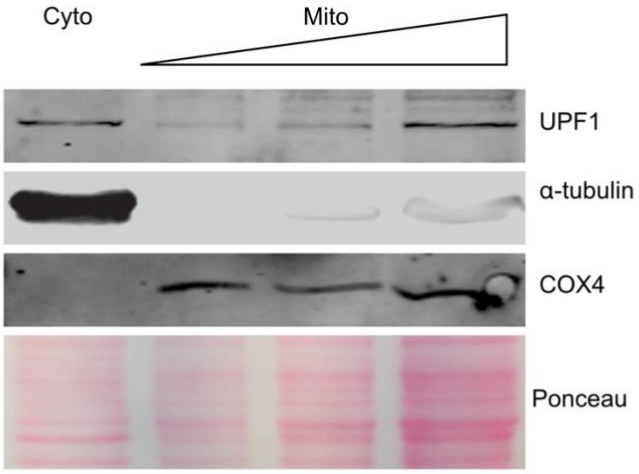

Figure S3. UPF1 colocalises and copurifies with COX4 in S2 cells. Co-fractionation western blot experiment of cytoplasmic (Cyto) and mitochondrial (Mito) fractions. Both fractions were stained for UPF1 alongside α-tubulin and COX4 as controls for the cytoplasm and mitochondria, respectively. Ponceau staining of the membrane serves as a loading control.

Figure S4

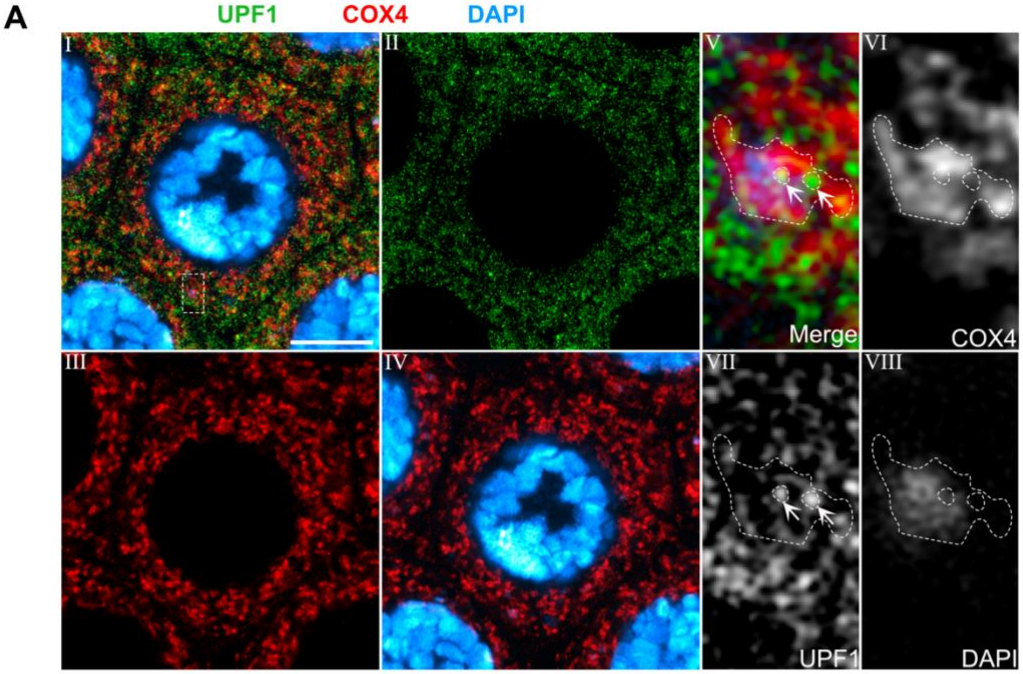

2nd Instar Larvae

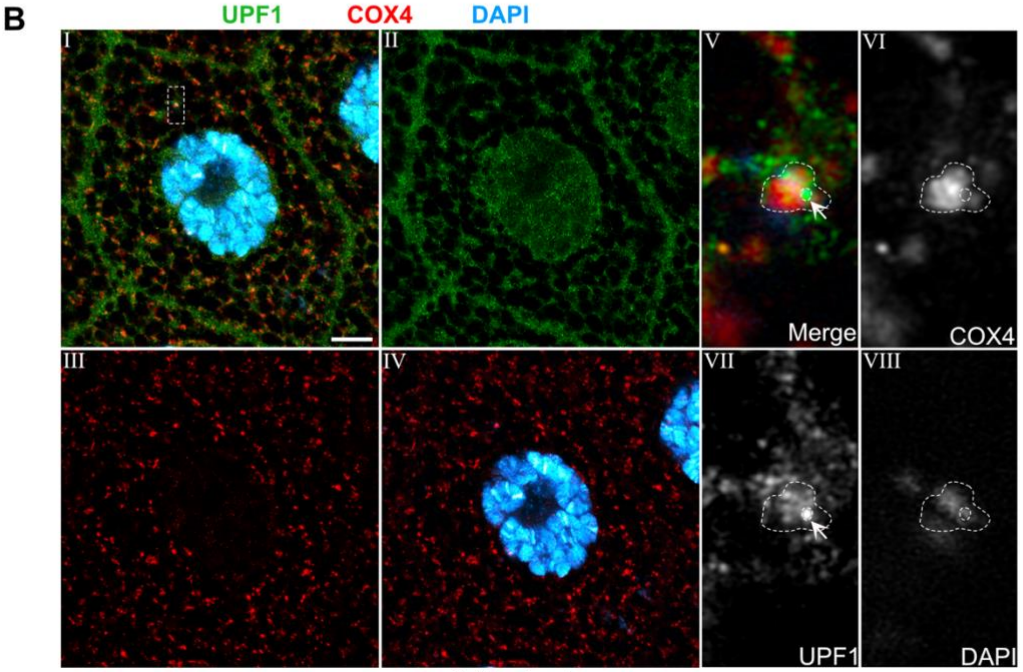

3rd Instar Larvae

Figure S4. Endogenous UPF1 colocalises with COX4 in salivary glands. Fluorescence immunolocalisation of endogenous UPF1 (green) and COX4 (red) as the mitochondrial marker. DAPI (blue) represents DNA (both nuclear and mtDNA). (**A**) Shows a second instar larva salivary gland cell. (**B**) A third instar larvae cell. In both instances, panel I represents a merged image of all three channels, UPF1 (panel II), COX4 (panel III). Panel IV represents both COX4 and DAPI. The boxed region is shown magnified in panels V-VIII, as merged (V) and grey panels for COX4 (VI), UPF1 (VII) and DAPI (VIII). Arrows point to foci of UPF1 adjacent to DAPI-stained regions of the mitochondria. Scale bar represents 10 µm.

Figure S5

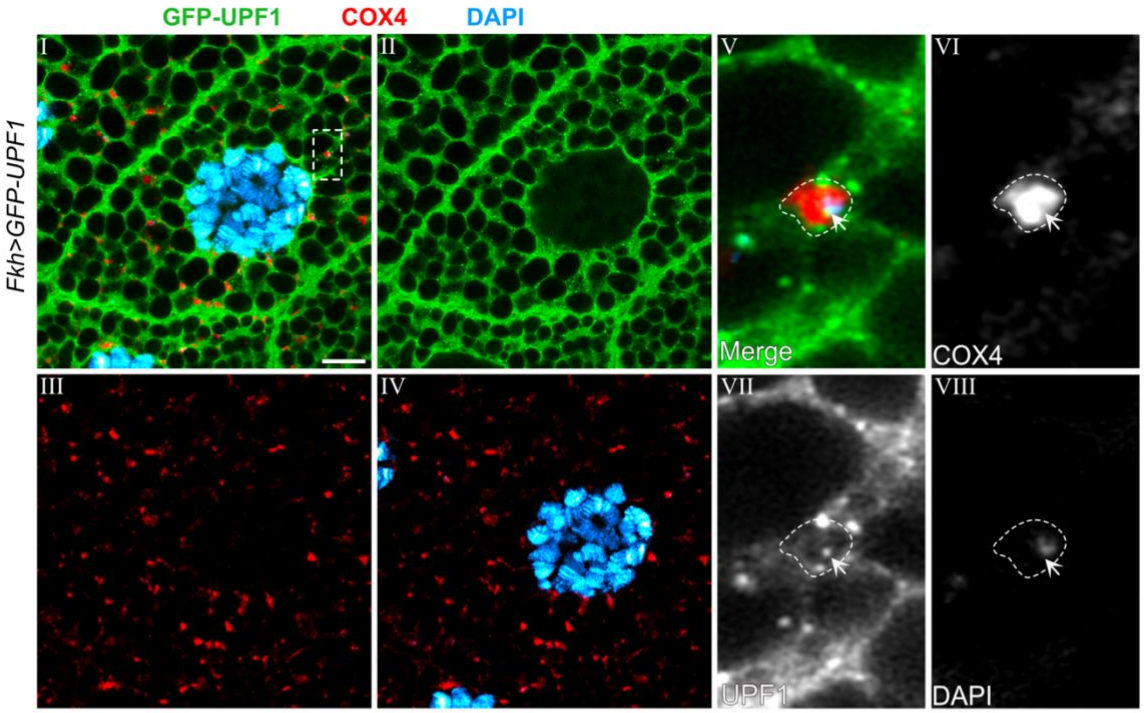
GFP-UPF1
COX4
DAPI
Fkh>GFP-UPF1
I
II
V
VI
Merge
COX4
III
IV
VII
VIII
UPF1
DAPI

Figure S5. GFP-tagged UPF1 localises to mitochondria in salivary glands. Fluorescence immunolocalisation of *FkhGAL4* driven expression of GFP-UPF1 (green) and immunostaining of endogenous COX4 (red). DAPI (blue) represents nuclear and mtDNA in third instar salivary glands. Panel I shows a merged image of all three channels, UPF1 (panel II), COX4 (panel III). Panel IV displays both COX4 and DAPI. The boxed region shown in panel I is shown in panels V-VIII, as merged (V) and grey panels for COX4 (VI), UPF1 (VII) and DAPI (VIII). Arrows point to foci of UPF1 adjacent to DAPI-stained regions of the mitochondria. Scale bar represents 10 µm.

Figure 2

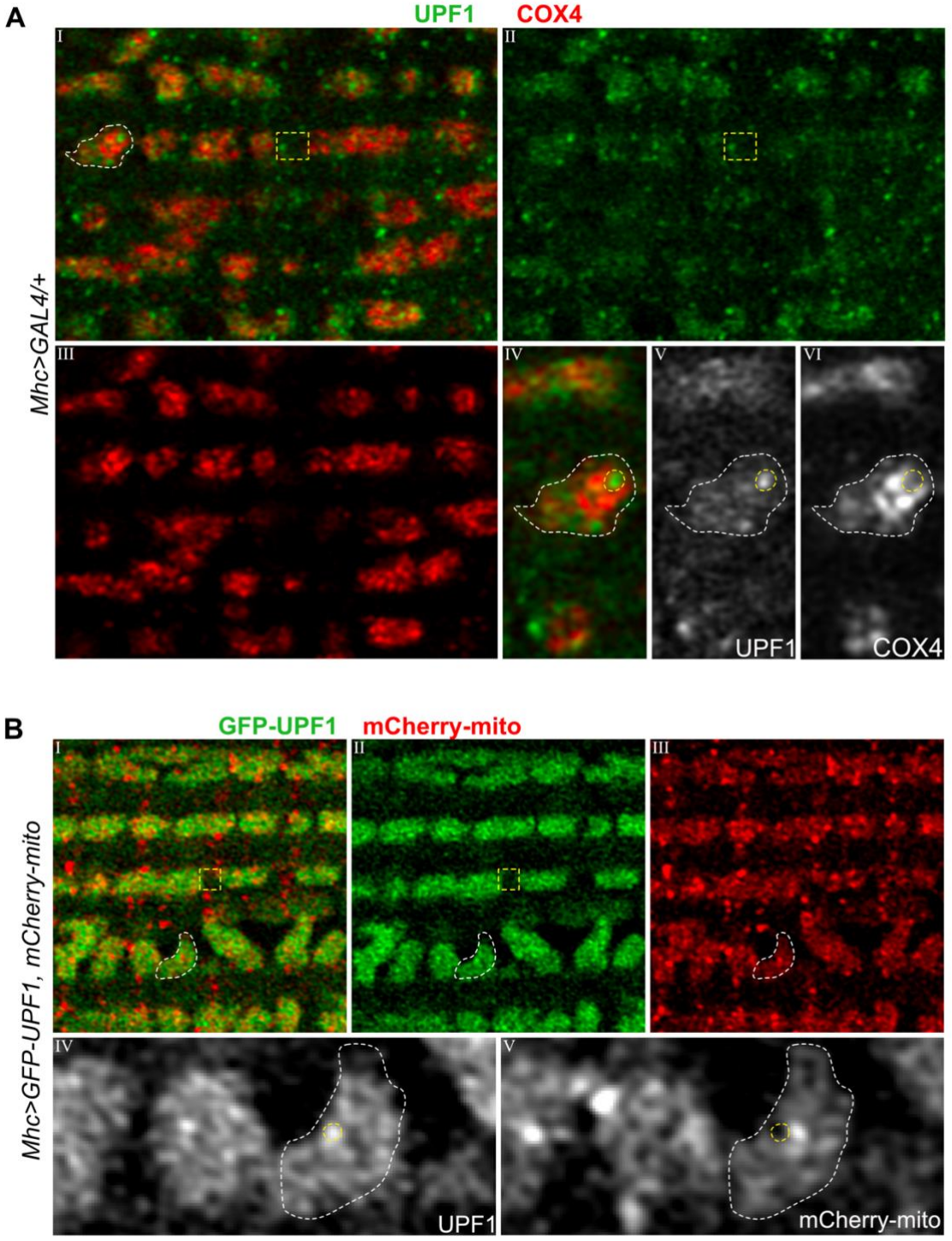
A
UPF1
COX4
Mhc>GAL4/+
I
II
III
IV
V
VI
UPF1
COX4
B
GFP-UPF1
mCherry-mito
Mhc>GFP-UPF1, mCherry-mito
I
II
III
IV
V
UPF1
mCherry-mito

Figure 2. UPF1 concentrates in mitochondria of the flight muscles. (**A**) Fluorescence immunolocalisation of endogenous UPF1 (green) and COX4 (red) as the mitochondrial marker in indirect flight muscles. Panel I represents a merged image of both channels, UPF1 (panel II) and COX4 (panel III), with an example cytoplasmic region indicated by the yellow dashed rectangle. Panels IV-VI represent a magnified view of the mitochondrial region outlined in panel I, as the merged image (panel IV), or as individual channels in grey, UPF1 (panel V) and COX4 (panel VI). A strong dot of UPF1 signal is circled in yellow within the selected mitochondrial region. This localises in a region lacking COX4 signal. (**B**) Fluorescence localisation of *MhcGAL4* driven expression of GFP-UPF1 (green) and mCherry-mito (red) in indirect flight muscles. Panel I represents a merged image of both channels, GFP-UPF1 (panel II) and mCherry-mito (panel III), a cytoplasmic region is indicated by the yellow dashed rectangle . Panels IV-V represent a magnified view of the mitochondrial region outlined in panel I, showing the individual channels UPF1 (panel IV) and mCherry-mito (panel V), in grey. A strong dot of UPF1 signal is circled in yellow within the selected mitochondrial region. This localises in a region without mCherry-mito signal.

Figure 3

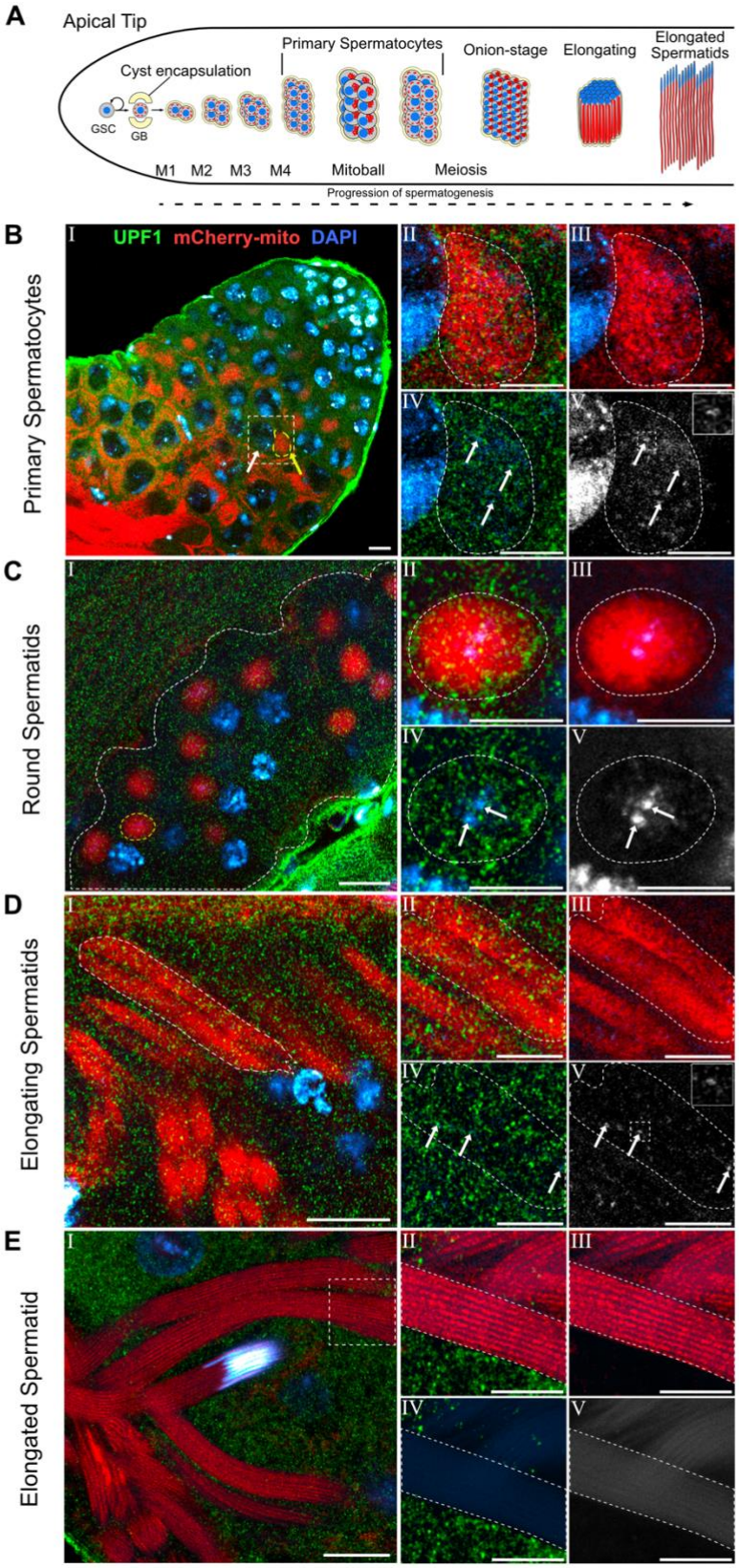
A
Apical Tip
Cyst encapsulation
GSC
GB
Primary Spermatocytes
Onion-stage
Elongating
Elongated Spermatids
M1
M2
M3
M4
Mitoball
Meiosis
Progression of spermatogenesis
B
Primary Spermatocytes
UPF1 mCherry-mito DAPI
C
Round Spermatids
D
Elongating Spermatids
E
Elongated Spermatid

Figure 3. UPF1 mitochondrial localisation during mitochondria clustering and fusion in developing spermatids. (**A**) Schematic representing *Drosophila* spermatogenesis. A germinal stem cell (GSC) at the apical tip of the testes proliferates into a differentiating gonialblast (GB), and a self-renewing GSC. The GB is enclosed by within a cyst made of two cyst cells and undergoes four rounds of mitosis (M1-M4) to produce 16 diploid primary spermatocytes. The mitochondria (red) cluster to form the Mitoball, a transient structure adjacent to the nucleus (blue). The mitoball disperses and the primary spermatocytes undergo meiosis to produce 64 haploid, round onion-stage spermatids, the mitochondria have fused to form the nebenkern adjacent to the nucleus. Each spermatid then undergoes elongation, with the unfurling of the nebenkern into the major and minor mitochondrial derivatives, and into the elongating tail. (**B-E**) Fluorescent immunolocalisation of endogenous UPF1 (green), imaging of ubiquitously expressed mCherry-mito (red) as the mitochondrial marker, and DAPI (blue) to stain nuclear and mitochondria DNA. (**B**) Primary spermatocytes. Panel I represents a merged image of the three channels, with a primary spermatocyte outlined with the white dotted box, the white arrow corresponds to the nucleus and the yellow arrow marks the Mitoball. Panel II represents the merged magnified view of the outlined primary spermatocyte in panel I, the Mitoball is outlined in white. Panel III – IV represent mCherry-mito (panel III) and UPF1 (panel IV) together with DAPI. Panel V shows DAPI alone, with a magnified inset showing a nucleoids, indicated by the top arrow (top right). White arrows in panels IV and V indicate UPF1 dots proximal to DAPI signal. (**C**) Shows a cyst with round-stage spermatids. Magnified views of the nebenkern outlined in yellow in panel I, are indicated in panels II-V. White arrows in panels IV and V point to two clusters of the mtDNA/nucleoids in the centre nebenkern. (**D**) Localisation in elongating spermatids. Magnified view of a portion of the area (major and minor mitochondrial derivatives) outlined by the dashed line in panel I are shown in panels II – V. Arrows in panels IV and V show dots of UPF1 adjacent to DAPI, magnification inset of DAPI is seen in panel V (top right). Panel V shows DAPI alone. Arrows in panels IV and V indicate UPF1 dots proximal to residual DAPI foci. (**E**) Imaging of elongated spermatids, which show absence of UPF1. Panel I shows the outlined region which is magnified in panels II-V which show absence of UPF1 and DAPI foci in the spermatid tail, panels IV-V. Scale bars in B-E, panel I represent 10 µm, scale bars in B-E, panels II-IV represent 5 µm.

Figure S6

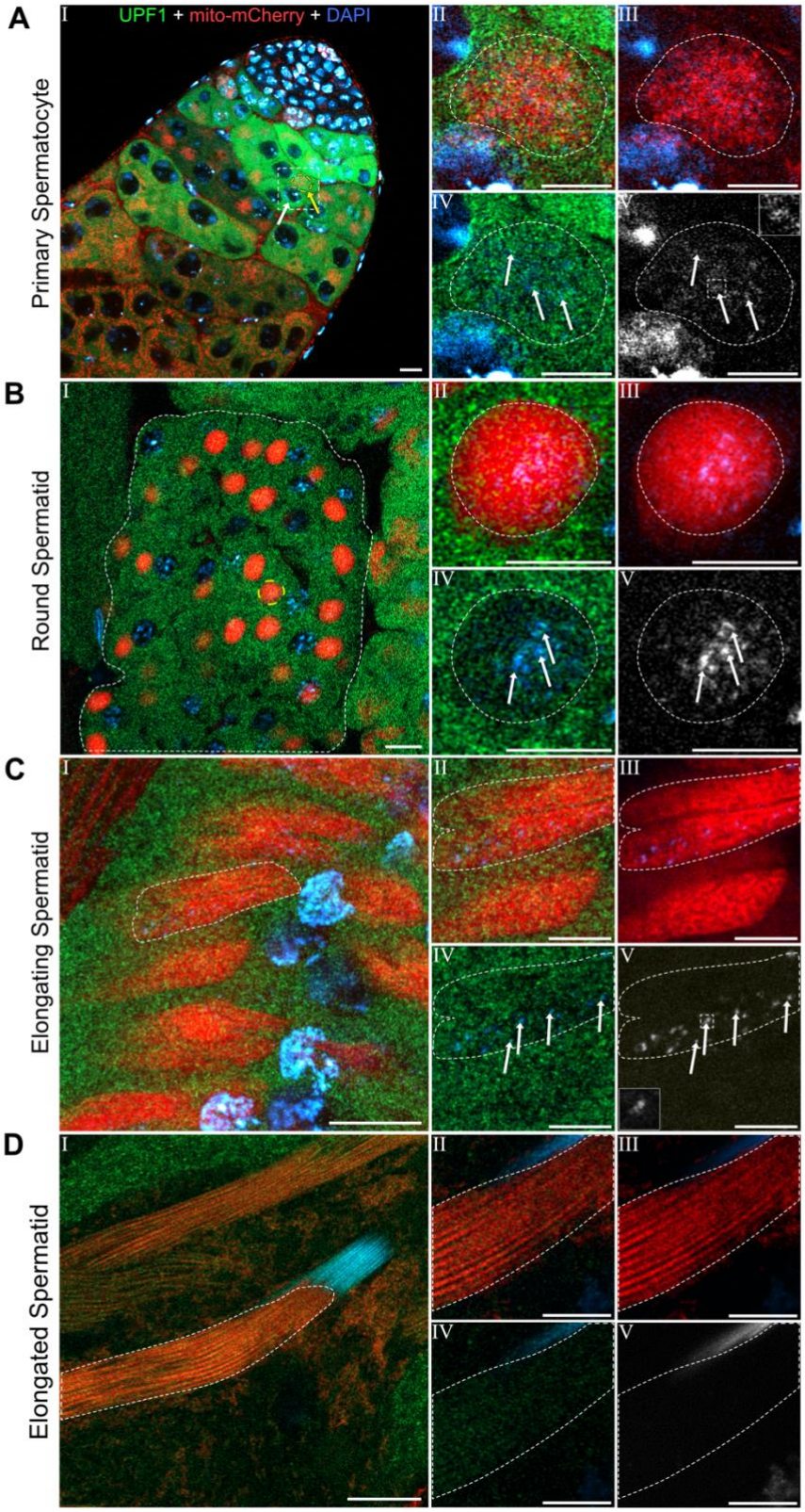
A
Primary Spermatocyte
UPF1 + mito-mCherry + DAPI
I
II
III
IV
V
B
Round Spermatid
C
Elongating Spermatid
D
Elongated Spermatid

Figure S6. GFP-UPF1 also localises to mitochondria in developing spermatids. (**A-D**) Fluorescent localization of GFP-UPF1 (green), ubiquitously expressed mCherry-mito (red) as the mitochondrial marker, and DAPI (blue) to stain nuclear and mitochondria DNA. (**A**) Primary spermatocytes. Panel I represents a merged image of the three channels, with a primary spermatocyte outlined with the white dotted box, the white arrow corresponds to the nucleus and the yellow arrow marks the Mitoball. Panel II represents the merged magnified view of the outlined primary spermatocyte in panel I, the mitoball is outlined by the dashed white line. Panel III – IV represent mCherry-mito (panel III) and GFP-UPF1 (panel IV) together with DAPI. Panel V shows DAPI alone, with a magnified inset panel showing an example of a nucleoid region (top right). Arrows in panels IV and V indicate strong UPF1 signal proximal to DAPI signal. (**B**) Shows a cyst with round-stage spermatids. Magnified views of the nebenkern outlined in yellow in panel I are shown in panels II-V. White arrows in panels IV and V indicate GFP-UPF1 dots adjacent to DAPI in in the centre nebenkern. (**C**) GFP-UPF1 localisation in elongating spermatids. Magnified view of a portion of the area (major and minor mitochondrial derivatives) outlined by the dashed line in panel I are shown in panels II – V. Arrows in panels IV and V show strong signals of GFP-UPF1 adjacent to DAPI, magnification inset of DAPI is seen in panel V (bottom left). Panel V shows DAPI alone. Arrows in panels IV and V indicate strong GFP-UPF1 signals proximal to DAPI signal. (**D**) Imaging of elongated spermatids, which show absence of GFP-UPF1. Panel I shows the outlined region which is magnified in panels II-V which show absence of GFP-UPF1 and DAPI foci in the spermatid tail, panels IV-V. Scale bars in B-E, panel I represent 10 µm, scale bars in B-E, panels II-IV represent 5 µm.

Figure 4

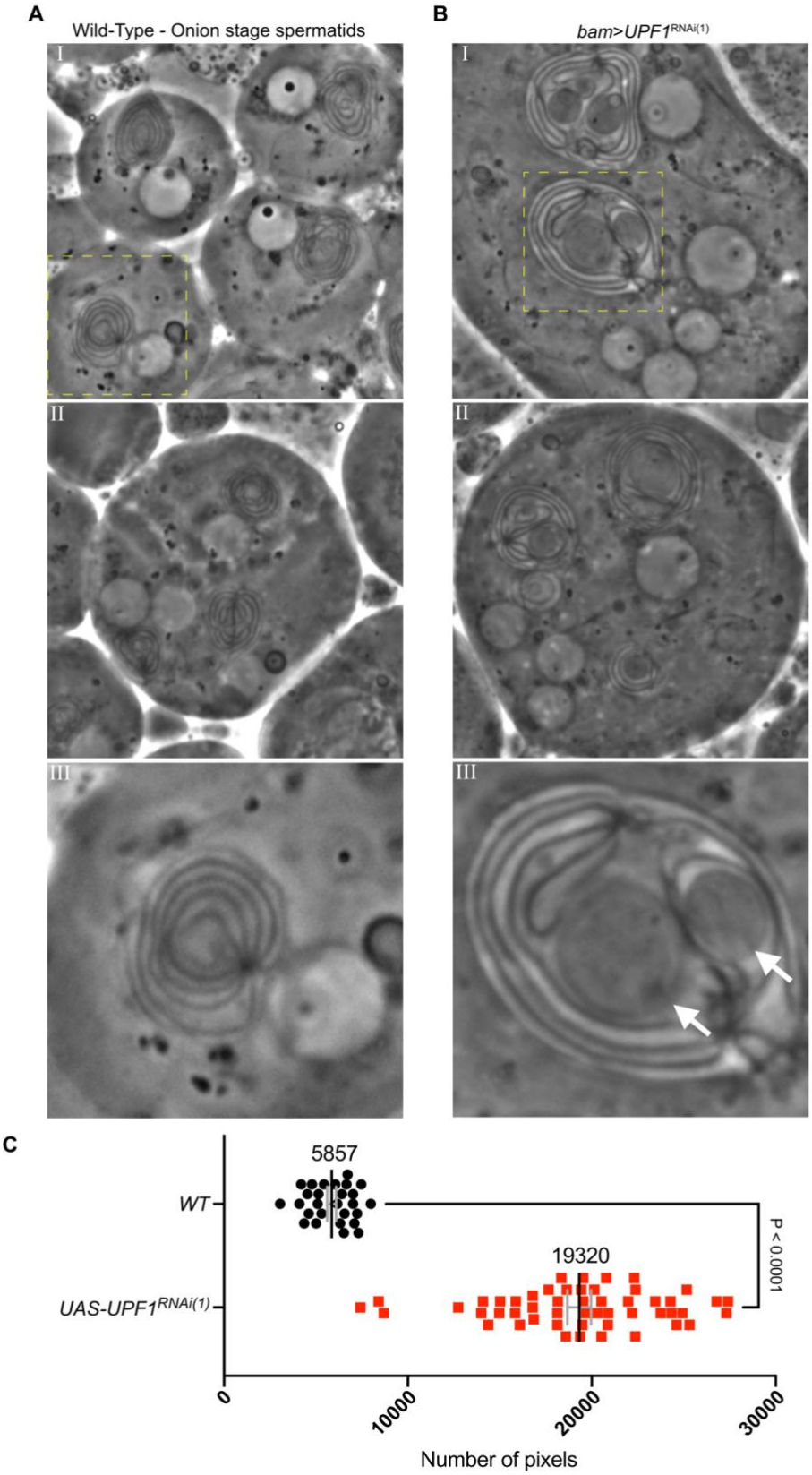
A
Wild-Type - Onion stage spermatids
B
bam>UPF1RNAi(1)
I
II
III
C
5857
WT
19320
UAS-UPF1RNAi(1)
P < 0.0001
0
10000
20000
30000
Number of pixels

Figure 4. Depletion of UPF1 in developing spermatids results in abnormal nebenkern formation and meiotic defects. (**A-B**) Phase contrast microscopy of round stage spermatids. (**A**) WT round stage spermatids. Panel I shows four distinct round spermatids. Panel II shows a syncytium-like structure containing four nuclei, each with an adjacent nebenkern. The magnified view of the yellow outlined region in panel I is shown in panel III below. (**B**) Round spermatids following *bamGAL4* driven $UPF1^{RNAi(1)}$. Panel I shows syncytium-like structure corresponding to several round stage spermatids, with nuclei of differing sizes and large nebenkern. Panel II shows a cyst of round stage spermatids, with a syncytium appearance. The magnified view of the abnormal nebenkern outlined in yellow in panel I is shown in panel III. Arrows in panel III indicate large, spheroid bodies within the nebenkern. (**C**) Quantification of nebenkern area (number of pixels) in WT and UPF1 depleted testes. Error bars represent the standard error of the mean. Statistical significance was calculated using a two-tailed unpaired parametric t-test and shown where the P-value < 0.05. RNAi efficiency was estimated by RT-qPCR using UPF1-specific primers. RNA was reduced to 30-40 % of control.

Figure S7

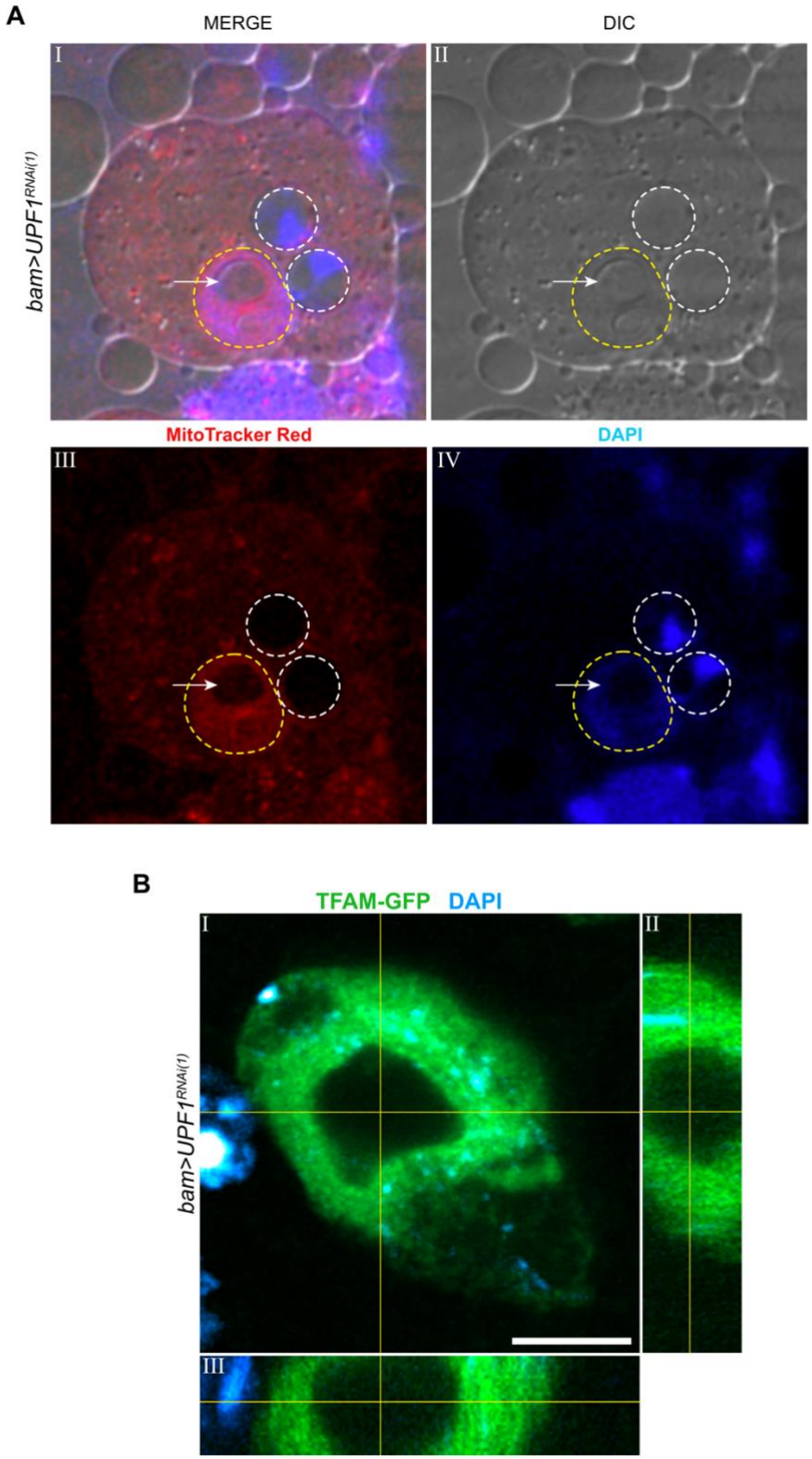
A
MERGE
DIC
I
II
bam>UPF1RNAi(1)
MitoTracker Red
DAPI
III
IV
B
TFAM-GFP DAPI
I
II
III
bam>UPF1RNAi(1)

Figure S7. The spheroid bodies within the UPF1KD nebenkern do not stain for DAPI. (**A**) DIC and fluorescent microscopy of round stage spermatid syncytium in *bam>UPF1*$^{RNAi(1)}$ testes, with MitoTracker Red CMXROS (red) as the mitochondrial marker, and DAPI (blue) to mark nuclear and mitochondrial DNA . Panel I represents the merged image of all channels, DIC (panel II), MitoTracker Red (panel III) and DAPI (panel IV). The nebenkern is outlined in yellow, whilst two adjacent nuclei are outlined in white. The spheroid bodies in the nebenkern are circled by dashed lines and one, yellow, indicated by the white arrow. The structure within the nebenkern does not stain with either MitoTracker Red (panel III) or DAPI (panel IV). (**B**) DAPI visualisation of mtDNA in *bamGAL4* driven *UPF1*$^{RNAi(1)}$. The nebenkern is marked by the expression TFAM-GFP (green) and contains mtDNA (blue), in the area not occupied by the spheroid body. Panel I is the central optical section of the nebenkern morphology, panel II and III show the orthogonal views of the region in the YZ and XZ planes, respectively.

Figure 5

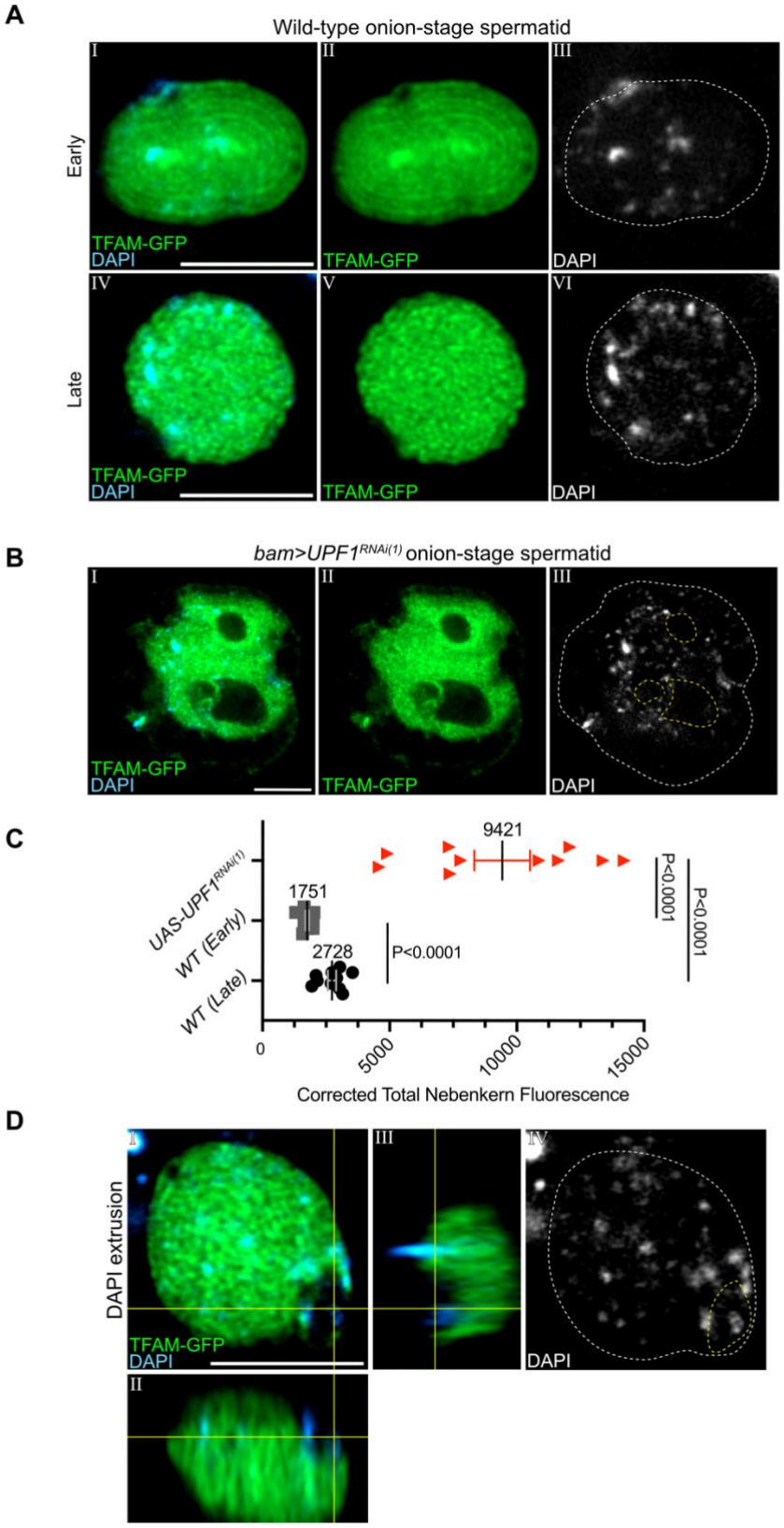
A
Wild-type onion-stage spermatid
Early
Late
I
II
III
IV
V
VI
TFAM-GFP
DAPI
B
bam>UPF1RNAi(1) onion-stage spermatid
C
UAS-UPF1RNAi(1)
WT (Early)
WT (Late)
1751
2728
9421
P<0.0001
P<0.0001
P<0.0001
0
5000
10000
15000
Corrected Total Nebenkern Fluorescence
D
DAPI extrusion

Figure 5. DNA-containing protrusions are formed at the nebenkern periphery in wild type but not in UPF1KD spermatids. Imaging of nebenkern in WT, and UPF1KD testes, using TFAM-GFP as the mitochondrial marker (green) and DAPI to stain DNA (blue). Scale bars all represent 5 µm. (**A**) WT early (panels I-III), and late (panels IV-VI) nebenkern morphology. Panels I and IV represent a merged image of the two channels, panels II, and V show TFAM-GFP, mtDNA is shown alone in grey in panels III and IV with the nebenkern outlined in white. (**B**) Nebenkern morphology in UPF1KD testes (panels I-III). Panel I shows a merged image of both channels. Panel II shows TFAM-GFP alone. Panel III shows mtDNA alone in grey with the nebenkern outlined in white, and vesicular bodies outlined in yellow. (**C**) Total corrected fluorescence quantification of mtDNA in the nebenkern in WT and UPF1KD testes. mtDNA was quantified for both stages of nebenkern seen in WT testes. Error bars represent the SEM. significance was calculated by using an unpaired t-test whereby $P \leq 0.05$. (**D**) WT nebenkern with vesicular-like structures at the periphery. Panel I shows a merged image of both channels, TFAM-GFP and DAPI. Panel II and III represent the orthogonal view of the XY and ZY planes, respectively. Panel IV shows DAPI alone in grey with the nebenkern and vesicular-like structure outlined in white and yellow, respectively.

Figure 6

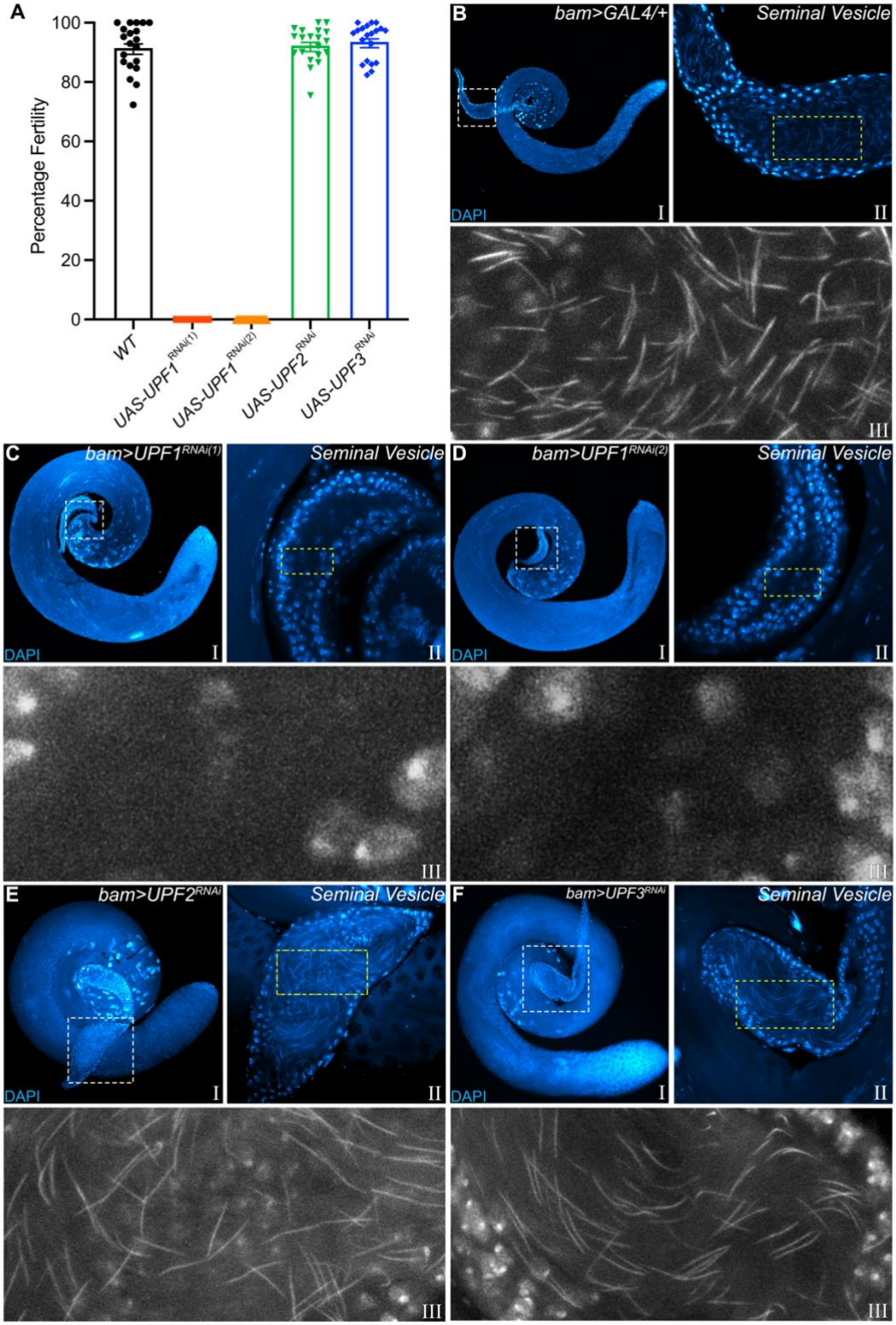
A
Percentage Fertility
100
80
60
40
20
0
WT
UAS-UPF1 RNAi(1)
UAS-UPF1 RNAi(2)
UAS-UPF2 RNAi
UAS-UPF3 RNAi
B
bam>GAL4/+
Seminal Vesicle
DAPI
I
II
III
C
bam>UPF1 RNAi(1)
Seminal Vesicle
DAPI
I
II
III
D
bam>UPF1 RNAi(2)
Seminal Vesicle
DAPI
I
II
III
E
bam>UPF2 RNAi
Seminal Vesicle
DAPI
I
II
III
F
bam>UPF3 RNAi
Seminal Vesicle
DAPI
I
II
III

Figure 6. Depletion of UPF1 but not other NMD factors causes male sterility. (**A**) Fertility scoring of males depleted of UPF1, UPF2 and UPF3 in testes crossed with wild type females. Percentage fertility calculated by: (number of pupa ÷ number of eclosed flies) ÷ number of egg-laying days. (**B-F**) Confocal images of DAPI-stained testes, to mark nuclear DNA. (**B**) WT testes (*bamGAL4:vp16)*, panel I. Panel II shows the seminal vesicle indicated in panel I by the white box. Panel III shows the magnified inset of the yellow box in panel II in grey, this is the content of the seminal vesicle with visible spermatid heads stained with DAPI (grey). (**C**) UPF1KD testes (*bam>UPF1*$^{RNAi(1)}$), panel I, show empty seminal vesicles (panel II) with no visible spermatids heads (panel III). (**D**) An empty seminal vesicle is seen again in a second line of UPF1KD (*bam>UPF1*$^{RNAi(2)}$; panels I-III). (**E**) UPF2KD testes (bam>*UPF2*^{RNAi}), panel I, demonstrate full seminal vesicles, with visible mature spermatid heads (panel II-III). (**F**) UPF3KD testes (*bam>UPF3*^{RNAi}), panel I, also shows mature spermatids in the seminal vesicle (panel II-III).

Figure 7

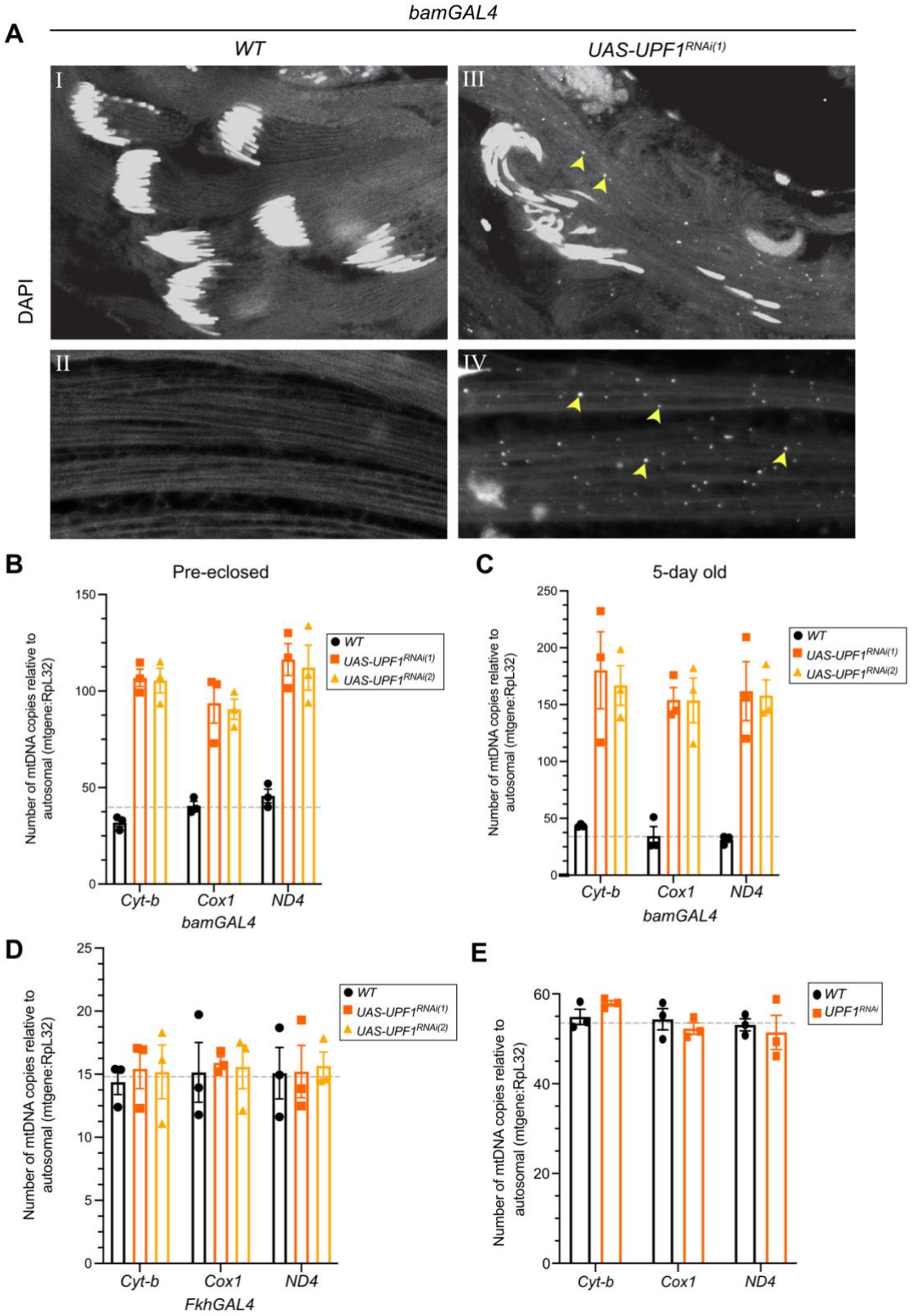
A
bamGAL4
WT
UAS-UPF1RNAi(1)
DAPI
I
II
III
IV
B
Pre-eclosed
Number of mtDNA copies relative to autosomal (mtgene:RpL32)
WT
UAS-UPF1RNAi(1)
UAS-UPF1RNAi(2)
Cyt-b
Cox1
ND4
bamGAL4
C
5-day old
D
FkhGAL4
E
UPF1RNAi

Figure 7. The elongated spermatids retain the mtDNA in UPF1KD. (**A**) DAPI-stained elongated spermatid bundles in WT (panels I-II) and *UPF1*$^{RNAi(1)}$ (panels III-IV) testes. Panels II and IV represent magnified view of bundles of elongated spermatid tails. In panel III and IV DAPI signals represent putative mtDNA/nucleotides, examples are indicated by yellow arrows. (**B-E**) RT-qPCR of total genomic DNA (gDNA), using three mitochondrial genome loci: *Cyt-b*, *Cox1* and *ND4*, and normalised against the autosomal locus, *RpL32*, to calculate a ratio of mtDNA copy number. (**B**) In WT and UPF1KD testes from pre-eclosed, (**C**) 5-day old testes, (**D**) salivary glands and (**E**) S2 cells. Two *UPF1*^{RNAi} lines were driven in testes (**B** & **C,** red (*UPF1*$^{RNAi(1)}$) and blue bars (*UPF1*$^{RNAi(2)}$), respectively) and salivary glands (**D**) using *bamGAL4* and *FkhGAL4*. dsRNA was transfected into S2 cells to induce UPF1^{RNAi} (**E**). Error bars represent SEM, significance was calculated by using an unpaired t-test whereby $P \leq 0.05$.

Figure S8

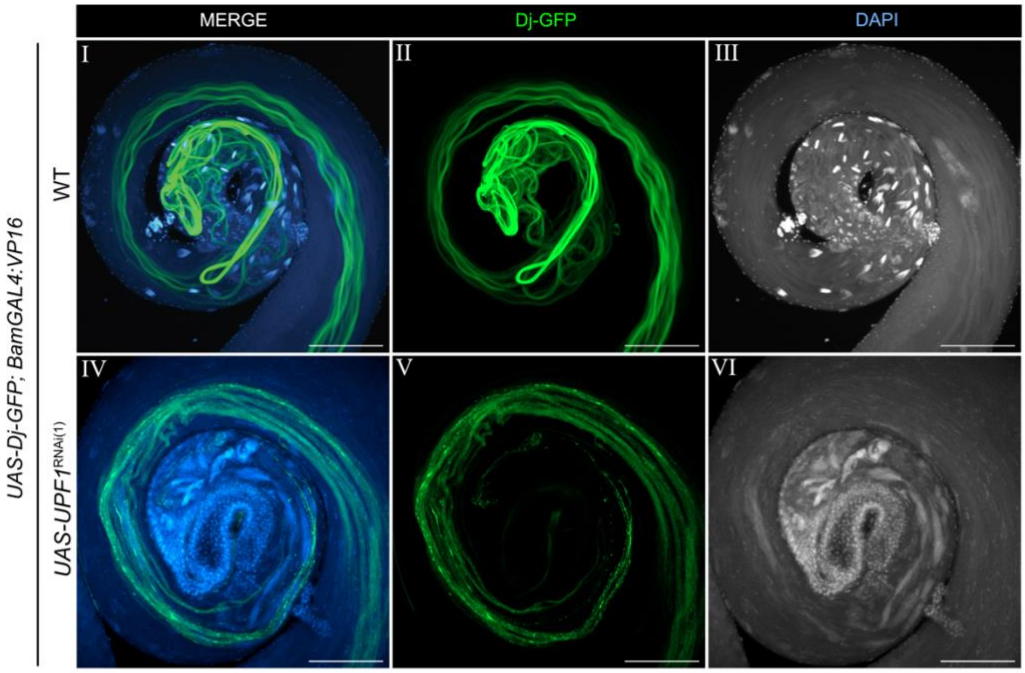
MERGE
Dj-GFP
DAPI
I
II
III
IV
V
VI
WT
UAS-UPF1RNAi(1)
UAS-Dj-GFP; BamGAL4:VP16

Figure S8. Fully elongated spermatids incorporating don juan (Dj) are produced in UPF1KD testes. Confocal microscopy of *bamGAL4* driven expression of Dj-GFP (green) and staining of DAPI to mark DNA (blue). WT testes (panel I) shows a merged image of both channels, with Dj-GFP marking the elongated spermatid tails (panel II) and DAPI marking the nuclei (panel III). Merged image of UPF1KD testes (panel IV), Dj-GFP and DAPI are shown separately (panel V and VI, respectively). Scale bar represents 100 µm.

Figure S9

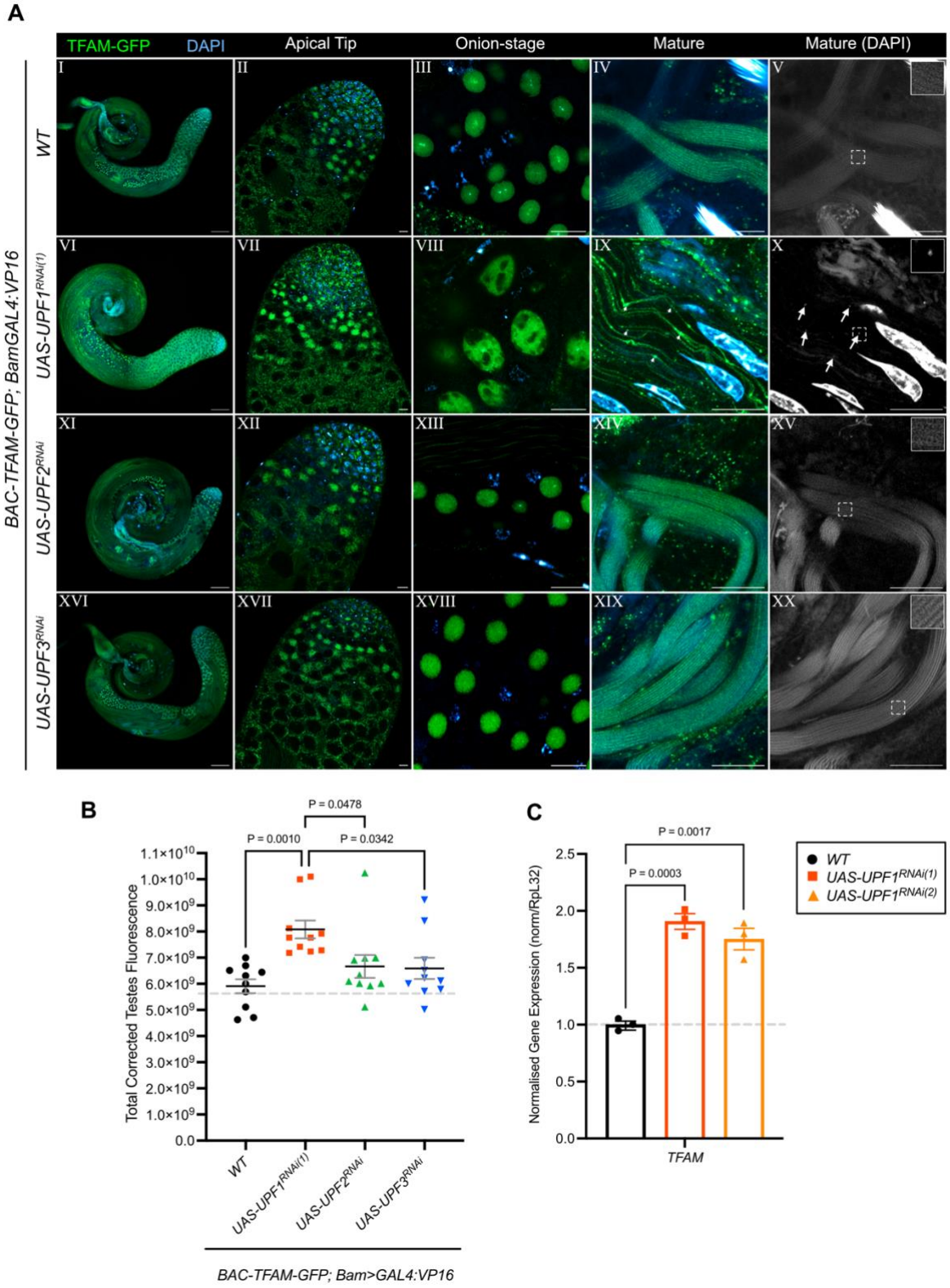
A
TFAM-GFP
DAPI
Apical Tip
Onion-stage
Mature
Mature (DAPI)
BAC-TFAM-GFP; BamGAL4:VP16
WT
UAS-UPF1RNAi(1)
UAS-UPF2RNAi
UAS-UPF3RNAi
I
II
III
IV
V
VI
VII
VIII
IX
X
XI
XII
XIII
XIV
XV
XVI
XVII
XVIII
XIX
XX
B
P = 0.0478
P = 0.0010
P = 0.0342
Total Corrected Testes Fluorescence
1.1×10^10
1.0×10^10
9.0×10^9
8.0×10^9
7.0×10^9
6.0×10^9
5.0×10^9
4.0×10^9
3.0×10^9
2.0×10^9
1.0×10^9
0.0
WT
UAS-UPF1RNAi(1)
UAS-UPF2RNAi
UAS-UPF3RNAi
BAC-TFAM-GFP; Bam>GAL4:VP16
C
P = 0.0017
P = 0.0003
Normalised Gene Expression (norm/RpL32)
2.5
2.0
1.5
1.0
0.5
0.0
TFAM
WT
UAS-UPF1RNAi(1)
UAS-UPF1RNAi(2)

Figure S9. DAPI signals co-localising with TFAM-GFP are observed in UPF1KD spermatid tails. (**A**) Fluorescence visualisation of TFAM-GFP in wild type (panels I-IV) and UPF1KD (panels VI-X), UPF2KD (panels XI-XV) and UPF3KD (panels XVI-XX) testes. TFAM-GFP serves as a mitochondrial marker and is apparent at nucleoids (green), tissues were also stained with DAPI to mark nuclear and mitochondrial DNA (blue). Merged views of whole testes (panels I, VI, XI and XVI), apical tip of the testes (panels II, VII, XII, and XVII), onion-stage spermatids (panels III, VIII, XIII, and XVIII) and elongated spermatids (IV, IX, XIV and XIX) are shown. DAPI alone is shown for elongated spermatids (panels V, X, XV and XX). Scale bar represents 10 µm. (**B**) Total corrected fluorescence (TCF) quantification of TFAM-GFP in WT and UPF1KD, UPF2KD, and UPF3KD testes. TFC is calculated by: integrated density - (area * mean of the background measurement). Error bars represent the SEM. Significance was calculated by ordinary one-way ANOVA analysis with Tukey correction for multiple comparisons. (**C**) RT-qPCR quantification of *TFAM* expression in WT and UPF1 depleted testes using two RNAi lines ($UPF1^{RNAi(1)}$ and $UPF1^{RNAi(2)}$) normalised against *RpL32* using $2^{-(\Delta\Delta CT)}$. Significance was calculated using a two-way unpaired t-test, values where $P \leq 0.05$ are shown.